A genetic polymorphism of *p19*^{Arf} in MSM/Ms confers resistance to tumor progression

（MSM/Ms 系統に存在する *p19*^{Arf} の多型は腫瘍悪性化を制御する）

千葉大学大学院医学薬学府

先端医学薬学専攻

（主任：永瀬　浩喜　教授）

齋藤　慈

Contents

4. Results ・・・

1. Abstract

Identification of the specific genetic variants responsible for increased susceptibility to familial or sporadic cancers remains important. Using a forward genetics approach to map such loci in a mouse skin cancer model, we previously identified a strong genetic locus, *Stmm3* (skin tumor modifier of MSM 3), conferring resistance to chemically induced skin papillomas on chromosome 4. Here we report the cyclin-dependent kinase inhibitor gene *Cdkn2a*/*p19*^{Arf} as a major responsible gene for the *Stmm3* locus. We provide evidence that the function of *Stmm3* is dependent on *p53* and that *p19*$^{Arf\ \mathrm{MSM}}$ confers stronger resistance to papillomas than *p16*$^{Ink4a\ \mathrm{MSM}}$ *in vivo*. In addition, we found that genetic polymorphism in *p19*^{Arf} between MSM/Ms (Val) and FVB/N (Leu) modifies the susceptibility to skin carcinogenesis. Moreover, we demonstrated that the *p19*$^{Arf\ \mathrm{MSM}}$ allele more efficiently activates the p53 pathway than the *p19*$^{Arf\ \mathrm{FVB}}$ allele *in vitro* and *in vivo*. Furthermore, we found novel (non-reported) polymorphisms in *CDKN2A* that are in the vicinity of a polymorphism in mouse *Cdkn2a* associated with the risk of human cancers in the Japanese population. Genetic polymorphisms in *Cdkn2a* and *CDKN2A* may modulate cancer risk in both mice and humans.

2. Introduction

Cancer risk is regulated by the environment and the complex influence of genetic background factors. The effects of high penetrance genetic variants are identified through studies of cancer occurrence in human families. On the other hand, cancer risk is mainly related to multiple low-penetrance cancer (sporadic cancers) susceptibility genes[1-3]. Sporadic cancers have major implications for the prediction of individual cancer risk. Therefore, the identification of sporadic tumor modifiers leads to prevention strategies or targeted therapy. In recent years, next generation sequencing has enabled us to perform a genome-wide association study (Case-control GWAS) using human samples. However, such studies involve a huge number of DNA samples from cancer patients, and an equal number of well-matched controls. Such studies are plagued by confounding factors, such as population heterogeneity, variability of environmental exposures, weak effects, and genetic interactions, and require a very large number of cases and controls to reach significance[4-7].

The susceptibility of the two-stage skin carcinogenesis model varies among mouse strains and the genetic approach has been employed to identify genes related to tumor-susceptibility[8, 9]. Using the genetic approach, several skin tumor-susceptibility loci were identified using commonly inbred strains or wild-derived strains[10-20], some of which

have clear translatability to cancer susceptibility in humans[1-23].

Previously, we reported that the Japanese wild-derived mouse strain MSM/Ms is dominantly resistant to two-stage skin carcinogenesis when crossed with susceptible FVB/N mice[14]. We identified a series of skin papilloma resistance loci, *Stmm* (Skin tumor modifier of MSM) loci using a forward genetics approach to map such loci in a mouse skin cancer model[14, 24, 25]. *Pth* (Parathyroid hormone) was recently identified as a responsible gene for *Stmm1* on chromosome 7[26]. We therefore focused on the *Stmm3* locus on chromosome 4. *Stmm3* was originally identified as a *p53*-dependent modifier locus[14]. We generated a series of sub-congenic lines to refine the locus to identify the gene responsible for the effects of the locus. *Cdkn2a*, a known tumor suppressor, was found in the *Stmm3* locus. Previous studies reported that *Pctr1* and *2* (Plasmacytoma resistance1 and 2) are plasmacytoma susceptibility loci, and *Cdkn2a* was suggested to be a corresponding gene for *Pctr1*[27, 28]. *Cdkn2a* is also a strong candidate gene for *Papg1* (Pulmonary adenoma progression 1). *Papg1* was mapped as a lung cancer susceptibility locus[29]. The *Cdkn2a* locus encodes two separate proteins, $p16^{Ink4a}$ and $p19^{Arf}$, which are generated from alternative open reading frames. $p16^{Ink4a}$ and $p19^{Arf}$, two distinct tumor suppressors, enhance the growth-suppressive functions of the retinoblastoma protein pRb and p53 protein, respectively. The separate promoters

upstream of exon1α (encoding $p16^{Ink4a}$) and exon1β (encoding $p19^{Arf}$) are induced by hyperproliferative signals generated by activated oncoproteins, triggering *RB*- and *p53*-dependent programs, respectively[30-31]. Deletion or epigenetic silencing of the $p16^{Ink4a}$/$p19^{Arf}$ locus is one of the most frequently observed events in cancer. Furthermore, previous reports suggested that polymorphisms in *CDKN2A* are associated with the risk or prognosis of several human cancers[32-41]. Accordingly, the *Cdkn2a* locus is considered to be a strong candidate for *Stmm3*.

In this study, we identified the cyclin-dependent kinase inhibitor gene *Cdkn2a*/$p19^{Arf}$ as a major responsible gene for the *Stmm3* locus. We provide evidence that the function of *Stmm3* is dependent on *p53*, and that $p19^{Arf\ MSM}$ confers stronger resistance to papillomas than $p16^{Ink4a\ MSM}$ *in vivo*. In addition, we found that the genetic polymorphism in $p19^{Arf}$ between MSM/Ms (Val) and FVB/N (Leu) modifies the susceptibility to skin carcinogenesis. Moreover, we demonstrated that the $p19^{Arf\ MSM}$ allele more efficiently activates the p53 pathway than the $p19^{Arf\ FVB}$ allele *in vitro* and *in vivo*. Furthermore, we found novel (non-reported) polymorphisms in *CDKN2A* in the vicinity of a polymorphism in mouse *Cdkn2a* that are associated with the risk of human cancers in the Japanese population. Thus, genetic polymorphisms in *Cdkn2a* and *CDKN2A* should modulate cancer risk in both mice and humans.

3. Materials and Methods

3-1 Generation of *p16*$^{Ink4a\ MSM}$ and *p19*$^{Arf\ MSM}$ allele knockout mice

p16$^{Ink4a\ MSM}$ and *p19*$^{Arf\ MSM}$ allele knockout mice were generated using CRISPR/Cas9. Cas9/sgRNA target sequences were designed from *p16*^{Ink4a} and *p19*^{Arf} genomic sequences (http://molossinus.nig.ac.jp/mog2; *p16*^{Ink4a}: GCC TCG AGT TCG CTT TCC TCG CGG and GGT ACG ACC GAA AGA GTT CGG GG, *p19*^{Arf}: GAG GTG CCT CAA CGC CGA AG GGG and GAG CTG CAC GCA CAG GTG CCG TGG). These sequences were cloned into the pX459 vector (Addgene). Using an ES cell line previously established from MSM/Ms[42], 5×10^6 cells and 40 μg of pX459 were mixed and electroporated using a Bio-Rad Gene Pulser (Bio-Rad, Hercules, CA) set at 400 V and 125 μF. After 24-48 hours of electroporation, the cells were selected with puromycin (4 μg/ml). ES cells were aggregated with ICR embryos, and the chimeric blastocysts were transferred into the uteri of pseudo-pregnant females. Knockout alleles were detected by PCR amplification. The following primers generated *p16*^{Ink4a}: Forward Primer; ACC ATC CTC AGA GGA AGG and Reverse Primer; ATC TGG GGT ATG CAT TTC, *p19*^{Arf}: Forward Primer; TGG GCG CCT CTG GGA AGC and Reverse Primer; CAG CCT CAC CGT GTG CAA. Off-target cleavage sites were predicted and

searched by CRISPR direct (http://crispr.dbcls.jp/). All potential off-target sites were PCR amplified and sequenced to confirm off-target effects. The primers for amplifying the off-target sites are listed in Table 1.

3-2 Mice and tumor induction

This experiment was carried out in strict accordance with the recommendations in the Guide for the Care and Use of Laboratory Animals by the Ministry of Education, Culture, Sports, Science, and Technology of Japan. The protocol was approved by the Committee on the Ethics of Animal Experiments of the Chiba Cancer Center (Permit Number: 13–18). All efforts were made to minimize pain. FVB/N mice were purchased from Japan Clea. MSM/Ms mice have been maintained in the experimental animal facility at Niigata University and Chiba Cancer Center for more than 20 years. Resistant [(FVB/N × MSM/Ms) F_1 × FVB/N] backcross mice were selected for further backcrossing to FVB/N mice for over at least 10 generations, ultimately leading to congenic mice containing the MSM allele of *Stmm3* in a FVB/N background. These mice were then crossed with *p53*-deficient mice[43] to generate $p53^{+/-}$congenic mice. In addition, $p19^{Arf}$-deficient mice (C57BL/6×129SvJ) were provided by Dr. kamijo[44]. $p19^{Arf}$-deficient mice were backcrossed to FVB/N mice or MSM/Ms mice for over at

least 10 generations to generate *p19*$^{Arf+/-}$ (FVB/N×MSM/Ms) F_1 mice. These mice were treated following the two-stage carcinogenesis protocol. At 8–10 weeks of age, the backs of mice were carefully shaved with an electric clipper. Two days after shaving, a single dose of DMBA (25 μg per mouse in 200 μl of acetone) was applied to the shaved dorsal back skin. One week after initiation, tumors were promoted with TPA (10 μg per mouse in 200 μl of acetone) twice weekly for 20 weeks. Papilloma number and size (mm in diameter) was recorded from 10 weeks to 20 weeks.

3-3 Construction of expression plasmids

The *p19*^{Arf} (FVB/N) cDNA vector was purchased from OriGENE (Rockville, MD, USA). This sequence was designed from the *p19*^{Arf} transcript sequence (Ensemble, ENSMUST00000044303). The MSM/Ms derived variant L149V was prepared using the PrimeSTAR mutagenesis basal kit (Takara Bio Inc., Kusatsu, Japan) according to the instructions provided by the manufacturer. The following primers generated the L149V variant: Forward Primer; GCG TTC CGC TGG GTG GTC TTT GTG TTC CGC TG and Reverse Primer; AAA CGC AAG GCG ACC CAC CAG AAA CAC. HA-tagged MSM/Ms and FVB/N sequences of p19^{Arf} were cloned into the pMSCVpuro vector (Clontech). The following primer sets were designed to clone into pMSCVPuro:

Forward Primer; TTA TGG GTC GCA GGT TCT TGG TCA CTG TGA GGA TTC AGC GCG CGG GCC G and Reverse Primer; TTC TAC TAA GCG TAA TCT GGA ACG TCG TAT GGG TAT GCC CGT CGG TCT GGG CG.

3-4 Cell culture and retrovirus infection

NIH/3T3 cells were cultured in Dulbecco's Modified Eagle's Medium (DMEM) (Sigma) containing 10% Fetal Bovine Serum (FBS) (CCB) and 1% Penicillin-Streptomycin mixed solution (Nacalai Tesque). PlatE ecotropic packaging cells were transfected with $p19^{Arf\ MSM}$-HA or $p19^{Arf\ FVB}$-HA using the FuGENE® Transfection Reagent (Promega) following the manufacturer's recommendation. The retrovirus-containing medium was collected 48 hours after transfection and supplemented with 4 μg/mL polybrene (MILLIPORE) to NIH/3T3 cells.

3-5 Quantitative real-time RT-PCR

Total RNA was isolated from the indicated cells using TRIzol (Invitrogen) in accordance with the manufacturer's protocol. cDNA was generated with the iScript™ Select cDNA Synthesis Kit (Bio-Rad) using 100 ng of DNase-pretreated total RNA. qRT-PCR was performed using GeneAce SYBR® qPCR Mix α Low ROX in accordance

with the manufacturer's protocol (NIPPON GENE). *p19^{Arf}* expression levels were measured using the Applied Biosystems® 7500 (Life Technologies) and normalized by *β-Actin*. The following primers generated *p19^{Arf}*: Forward Primer; GTC GCA GGT TCT TGG TCA CT and Reverse Primer; GCC CTC TTC TCA AGA TCC TCT, *β-Actin*: Forward Primer; ACC TCA TGA AGA TCC TGA CC and Reverse Primer; CGT TGCC AAT AGT GAT GAC C, *p21*: Forward Primer; CCA CTT TGC CAG CAG AAT AA and Reverse Primer; ACG GGA CCG AAG AGA CAA C, *Noxa*: Forward Primer; GCA GAG CTA CCA CCT GAG TTC and Reverse Primer; CTT TTG CGA CTT CCC AGG CA, *Bax*: Forward Primer; CTG AGC TGA CCT TGG AGC and Reverse Primer; GAC TCC AGC CAC AAA GAT G.

3-6 SYBR Green real-time genomic PCR

Genomic PCR was performed using GeneAce SYBR® qPCR Mix α Low ROX in accordance with the manufacturer's protocol (NIPPON GENE) and as described previously[45]. The DNA solution comprised approximately 10 ng of genomic DNA. The following primers generated *p53*: Forward Primer; ACT CTC CTC CCC TCA ATA AGC and Reverse Primer; GCA GCG TCT CAC GAC CTC, *β-Actin*: Forward Primer; ACC TCA TGA AGA TCC TGA CC and Reverse Primer; CGT TGCC AAT AGT GAT

GAC C.

3-7 Cell cycle analysis

NIH/3T3 cells were cultured for 24 hours after being treated with DMSO (0.1%) or TPA (100 ng). Mouse keratinocytes were isolated from TPA (10 μg per mouse in 200 μl of acetone)-treated mice. Isolation of keratinocytes from mice was performed as described previously[46]. They were then collected and fixed in 70% ethanol at 4°C for 30 min. The fixed cells were stained with propidium iodide (50 μg/mL) containing 200 μg of RNaseA/mL and 1% Triton at 37°C for 40 min. Flow cytometry was conducted with JSAN (Japan-made sorter, analyzer) (Bay Bioscience). Approximately 1.0×10^5 cells were scanned to analyze DNA content. Necrotic cells were excluded, and the percentage of cells in the G_1, S, and G_2/M phases was determined.

3-8 Immunoblotting

Proteins were extracted from cells using the T-PER Protein Extraction Reagent (Thermo). Protein concentrations were quantified with the Quick Start Bradford Protein Assay (Bio-Rad). Denatured proteins (mouse skins: 60 μg, NIH/3T3 cells: 20 μg) were then analyzed using 15% e-PAGELs (ATTO). After electrophoresis, they were

transferred to polyvinylidene difluoride (PVDF) membranes (Merck Millipore). The membranes were blocked with 0.5% skim milk or 1% BSA in phosphate buffered saline solution (pH 7.6) containing 0.1% Tween-20 (PBS/T), and then analyzed with the SNAPi.d. 2.0 Protein Detection System (Merck Millipore). Primary antibodies were as follows: anti-$p19^{Arf}$ (1:500 5-C3-1, Santa Cruz), anti-HA (1:1000 16B12, BioLegend), anti-MDM2 (1:1000 SMP 14, abcam), anti-p53 (1:1000 PAb421, Merck Millipore), anti-ACTIN (Sigma-Merck Millipore). HRP-conjugated secondary antibodies were used at a dilution of 1:2000 and developed using the ECL Prime Western Blotting Detection Kit (GE Healthcare). Exposure for chemiluminescent samples or membrane analysis for the blots was performed by LAS4000 (GE Healthcare).

3-9 Subcellular localization assay

Subcellular fractionation of NIH/3T3 cells was carried out using the NE-PER Nuclear and Cytoplasmic Extraction Reagent (Thermo). In order to analyze $p19^{Arf}$ protein distribution in the nuclear and cytoplasmic compartments, an equal number of cells and nuclei were processed following the manufacturer's protocol. To verify the purity of the subcellular fractionation, anti-α-Tubulin (1:2000 DM1A, Cell Signaling) antibody and anti-Histone H3 (1:1000 D1H2, Cell Signaling) antibody were used for

immunoblotting.

3-10 Immunoprecipitation

Lysates (cytoplasmic extracts: 600 μg, nuclear extracts: 300 μg) were precleared with control agarose resin (Pierce) at 4°C for 60 min on a shaker. The binding of anti-MDM2 (10 μg; SMP 14, abcam) antibody to protein A/G agarose was performed following the protocol described in the Pierce crosslink immunoprecipitation kit (Thermo). The antibody-crosslinked beads were incubated overnight at 4°C with precleared lysates. After the incubation, the beads were washed three times with lysis/wash buffer, and the eluted complex was subjected to SDS-PAGE separation and immunoblotting.

3-11 Immunofluorescence

Samples were fixed with 4% paraformaldehyde at 4°C overnight. The endogenous peroxidase activity in the specimens was blocked by 0.3% H_2O_2 and samples were then rinsed with PBS. Sections were incubated with primary antibodies diluted in blocking buffer overnight at 4°C, and stained with anti-Ki67 (1:100 16A8, Biolegend), anti-keratin 14 (1:500 Poly19053, Biolegend), anti-Vimentin (1:100 EPR3776, abcam),

anti-E-cadherin (1:200 24E10, Cell Signaling), anti-HA (1:100 C29F4, Cell Signaling), anti-GAPDH (1:100 ab9485, abcam) antibody. The secondary antibodies were Alexa Fluor 488-conjugated anti-rat antibody (1:100, Molecular Probes, Invitrogen) and Alexa Fluor 568-conjugated anti-rabbit antibody (1:100, Molecular Probes, Invitrogen). Nuclei were counterstained with Hard Set Mounting Medium with DAPI (Vector). All fluorescence images were obtained with a Leica TCS SPE confocal microscope equipped with a DMI400B (10×/0.40, 20×/0.70, and 40×/1.25 oil immersion objective).

3-12 Samples and genotyping

All DNA samples used in the association analysis were obtained from Biobank Japan (Table 2). In this study, we used genotyping results of 6 cancers and non-cancer controls from previous studies by Illumina HumanHap610-Quad Beadchip (PMID: 20139978). Only male and female cases or non-cancer control samples were used for the analyses of prostate and breast cancer, respectively. All participants provided written informed consent. We selected five SNPs within the *CDKN2A* locus and conducted the association analysis. The associations between each SNP and the 6 cancers were assessed using the logistic regression analysis using age and gender as covariates. The significance thresholds were set to be 0.05/30= 0.00167 after Bonferroni correction.

3-13 Statistical analysis

All experiments were performed at least three times. Difference among multiple groups was calculated by one- and two-way ANOVA. Kaplan–Meier survival curve was analyzed by Log-rank test. These analyses used GraphPad Prism (GraphPad, San Diego, CA, USA).

4. Results

4-1 Congenic mice strains with MSM/Ms alleles of genes surrounding *Cdkn2a* are resistant to larger papillomas. Using initial generations of congenic mouse strains, we refined the location of the *Stmm3* locus within a physical interval of approximately 34 Mb on the distal end of chromosome 4[25]. To further narrow down the *Stmm3* locus, we generated *Stmm3* sub-congenic mouse lines covering the extended region, including the *Cdkn2a* locus (Figure. 1a). First, $p53^{+/+}$heterozygous FVB/MSM (F/M) and $p53^{+/+}$homozygous FVB/FVB (F/F) congenic mice were subjected to a DMBA/TPA skin carcinogenesis experiment according to the standard protocol, and papilloma development was monitored for a period of 20 weeks. $p53^{+/+}$F/M mice exhibited strong suppressive effects on papilloma development compared with $p53^{+/+}$F/F mice at 20 weeks after initiation (Figure. 1b, d). As a result, the *Stmm3* region was narrowed down to 88-93 Mb (5 Mb) on chromosome 4 by sub-congenic mapping analysis.

In our previous report, we concluded that *Stmm3* genes function mainly involved in late stage papillomas (>6 mm in diameter), but have weaker effects in early stage papillomas (≤6 mm in diameter) such as in papilloma development[14]. We classified papillomas of sub-congenic mice into two categories based on size. $p53^{+/+}$F/M mice

developed almost no late stage papillomas and *p53*$^{+/+}$F/F mice developed late stage papillomas (Figure. 1c, d). These results suggest that the corresponding gene responsible for tumor development and growth is contained within the *Stmm3* locus. In addition, we performed cell cycle analysis of TPA-treated skins of F/M and F/F mice, and found that untreated skins of F/M and F/F mice exhibited almost no cell cycle abnormalities (Figure. 2a, b). On the other hand, the percentage of cells in the G_0/G_1 phase was significantly higher and the percentage of cells in the S phase was significantly lower in TPA-treated skins of F/M mice than those in TPA-treated skins of F/F mice (Figure. 2a, b). These results suggest that the *Stmm3* locus induces G_1 arrest in mouse skin following TPA treatment.

4-2 The *Stmm3* locus regulates tumor progression in a *p53*-dependent manner. In our previous report, we demonstrated a genome-wide significant linkage at *Stmm3* on chromosome 4. However, this linkage peak at *Stmm3* completely disappeared in *p53*$^{+/-}$ mice. Therefore we concluded that *Stmm3* corresponding genes are genetically *p53*-dependent[14]. In this study, we generated *p53*$^{+/-}$ and *p53*$^{+/+}$ sub-congenic mouse lines for *Stmm3*. These mice were subjected to two-stage skin carcinogenesis using DMBA/TPA. *p53*$^{+/-}$F/M mice exhibited weakly affected papilloma development

compared with *p53*$^{+/-}$F/F mice (Figure. 3a, c).

Next, we examined the size of papillomas in *p53*$^{+/-}$sub-congenic mice as well as in *p53*$^{+/+}$ mice. The skin carcinogenesis experiments revealed that both *p53*$^{+/-}$F/M and *p53*$^{+/-}$F/F mice developed late stage (larger than 6 mm in diameter) papillomas (Figure. 3b, c). In contrast, when we measured the size of papillomas in *p53*$^{+/+}$sub-congenic mice, only *p53*$^{+/+}$ F/F mice developed late stage papillomas and the size difference between F/M and F/F mice was significantly larger in *p53*$^{+/+}$ than in *p53*$^{+/-}$ (Figure. 1 b, Figure. 3b). Thus, the *Stmm3* region exerted stronger suppressive effects on papillomas in the presence of two copies of *p53*, indicating that the effects of *Stmm3* are dependent on *p53*. We then carried out histological analysis of papillomas from *p53*$^{+/-}$sub-congenic mice. No morphological change or significant difference between *p53*$^{+/-}$F/M and *p53*$^{+/-}$F/F mice was noted on HE (hematoxylin and eosin) staining or immunohistochemical analysis with the cell proliferation marker Ki67 (Figure. 4a-e).

p53 heterozygosity has been reported to be associated with a higher frequency of progression to carcinomas without affecting papilloma development[47]. However, in order to eliminate the possibility that deletion of *p53* promotes papillomagenesis in *p53*$^{+/+}$F/F mice, we examined the *p53* allele using papillomas from F/M mice and F/F mice. We found that the *p53* allele level in papillomas was similar between *p53*$^{+/+}$F/M

and *p53*$^{+/+}$F/F mice (Figure. 5). Therefore, the *p53* allele was not deleted in papillomas from *p53*$^{+/+}$F/F mice and the effects of the *Stmm3* locus were dependent on *p53*.

4-3 A candidate gene for *Stmm3, Cdkn2a/p19*^{Arf}. Our animal experiments demonstrated that the *Stmm3* locus regulated tumor progression in a *p53*-dependent manner. The *p53*-dependent tumor suppressor gene *Cdkn2a*/*p19*^{Arf} was found to be located in the minimal congenic interval (Figure. 1a). Therefore, we initially focused on *Cdkn2a*/*p19*^{Arf}.

A previous report suggested that *p19*^{Arf} expression was regulated by TPA in mouse skin[48]. In addition, *p19*^{Arf} was not expressed in mouse skin in the absence of TPA. Therefore, we examined the *p19*^{Arf} expression levels using TPA-treated mouse skin from sub-congenic mice (M/M and F/F mice), and found that *p19*^{Arf} expression was almost the same in M/M and F/F mice (Figure. 6a). In addition, we measured the *p19*^{Arf} expression levels using TPA treated mouse skin from *p19*$^{Arf+/-}$ (FVB/N×MSM/Ms) F_1 mice, and found that *p19*^{Arf} expression was almost the same in *p19*$^{Arf\,-/MSM}$ (*p19*$^{Arf\,FVB}$ allele knockout F_1) and *p19*$^{Arf\,FVB/-}$ (*p19*$^{Arf\,MSM}$ allele knockout F_1) mice (Figure. 6b). On the other hand, according to the database (http://molossinus.lab.nig.ac.jp/msmdb/index.jsp), a genetic variant is located in exon 2

(149 aa) of the *Cdkn2a*/*p19*^{Arf} locus between MSM/Ms (Val) and FVB/N (Leu) (Figure. 6c). Therefore, we hypothesized that a nonsynonymous substitution in *p19*^{Arf} rather than expression was more likely to play a role in the modification of tumor resistance.

4-4 *p19*$^{Arf\ MSM}$ allele confers resistance to papilloma development. In this study, we considered *Cdkn2a*/*p19*^{Arf} to be one of the important modifier genes of skin carcinogenesis because of its *p53* dependency. However, the *Cdkn2a* locus encodes two separate proteins (Cdkn2a, also known as p16^{Ink4a}, and p19^{Arf}) generated from alternative open reading frames. Accordingly, we knocked out the *p16*$^{Ink4a\ MSM}$ and *p19*$^{Arf\ MSM}$ alleles using CRISPR/Cas9 in the (FVB/N×MSM/Ms) F_1 background and generated *p16*$^{Ink4a\ FVB/-}$ (*p16*$^{Ink4a\ MSM}$ allele knockout F_1) and *p19*$^{Arf\ FVB/-}$ (*p19*$^{Arf\ MSM}$ allele knockout F_1) mice. These mice were subjected to two-stage skin carcinogenesis using DMBA/TPA, and papilloma development was monitored for a period of 20 weeks. As a result, *p19*$^{Arf\ FVB/-}$ mice exhibited a significantly higher number of papilloma compared with *p19*$^{Arf\ FVB/MSM}$ (Figure. 7a). On the other hand, *p16*$^{Ink4a\ FVB/-}$ mice had minimal change in the papilloma number compared with *p16*$^{Ink4a\ FVB/MSM}$ (Figure. 7b). These results suggested that the *p19*$^{Arf\ MSM}$ allele conferred tronger resistance to papilloma number compared with the *p16*$^{Ink4a\ MSM}$ allele. Thus, *p19*^{Arf} was more likely to

be a *Stmm3* responsible gene than $p16^{Ink4a}$. Based on these results, we separately knocked out $p19^{Arf\ MSM}$ and $p19^{Arf\ FVB}$ in a (FVB/N×MSM/MS) F_1 background, and generated $p19^{Arf\ FVB/-}$ ($p19^{Arf\ MSM}$ allele knockout F_1) and $p19^{Arf\ -/MSM}$ ($p19^{Arf\ FVB}$ allele knockout F_1) mice in order to investigate the functions of the $p19^{Arf\ MSM}$ and $p19^{Arf\ FVB}$ alleles (Figure. 7c). These mice were subjected to DMBA/TPA skin carcinogenesis, and papilloma development was monitored for a period of 20 weeks. As a result, $p19^{Arf\ FVB/-}$ mice exhibited a significantly higher number of papilloma compared with $p19^{Arf\ -/MSM}$ and $p19^{Arf\ FVB/MSM}$ mice (Figure. 7 d, f). In addition, $p19^{Arf\ FVB/-}$ mice developed a significantly higher number of late stage (>6 mm) papillomas compared with $p19^{Arf\ -/MSM}$ and $p19^{Arf\ FVB/MSM}$ mice (Figure. 7e). These results demonstrate that the MSM allele of $p19^{Arf}$ suppresses papilloma development and growth more than the FVB allele, confirming $p19^{Arf}$ as a responsible gene for *Stmm3*.

We next performed histological analysis using papillomas from $p19^{Arf\ FVB/-}$, $p19^{Arf\ -/MSM}$, and $p19^{Arf\ FVB/MSM}$ mice. As HE staining revealed no significant morphological changes among these mice (Figure. 8a-c), we carried out immunohistochemical analysis with the cell proliferation marker Ki67. As a result, papillomas from $p19^{Arf\ FVB/-}$ mice had a significantly higher number of Ki67-positive cells, compared with that in papillomas from $p19^{Arf\ -/MSM}$ and $p19^{Arf\ FVB/MSM}$ mice (Figure. 8d-g). These results

suggest that the $p19^{Arf\ MSM}$ allele downregulates papilloma development by reducing proliferative cells.

4-5 The $p19^{Arf\ MSM}$ allele controls malignant conversion. In order to investigate the effects of $p19^{Arf\ MSM}$ and $p19^{Arf\ FVB}$ alleles on malignant conversion in $p19^{Arf\ FVB/-}$, $p19^{Arf\ -/MSM}$, and $p19^{Arf\ FVB/MSM}$ mice, we monitored carcinoma development up to 40 weeks after initiation. As a result, $p19^{Arf\ FVB/-}$ mice had a significantly higher incidence of papillomas compared with $p19^{Arf\ -/MSM}$ and $p19^{Arf\ FVB/MSM}$ mice (Figure. 9a). Furthermore, the survival rate of $p19^{Arf\ FVB/-}$ mice was significantly lower than that of $p19^{Arf\ -/MSM}$ mice and $p19^{Arf\ FVB/MSM}$ mice (Figure. 9b). These results suggest that $p19^{Arf\ MSM}$ strongly suppresses malignant conversion to carcinoma and prolongs the survival of mice compared with $p19^{Arf\ FVB}$.

Next, we performed histological analysis using carcinomas from $p19^{Arf\ FVB/-}$, $p19^{Arf\ -/MSM}$, and $p19^{Arf\ FVB/MSM}$ mice. Since HE staining revealed no significant morphological changes among these mice (Figure. 10a-l), we then carried out immunohistochemical analysis with the mesenchymal marker vimentin and the epithelial marker K14 and E -cadherin. As a result, carcinomas from $p19^{Arf\ FVB/-}$ mice had a significantly higher number of vimentin-positive cells than papillomas from $p19^{Arf\ -/MSM}$ and $p19^{Arf\ FVB/MSM}$

mice (Figure. 11a-m). On the other hand, carcinomas from $p19^{Arf\ FVB/-}$ mice had a significantly lower number of K14-positive cells compared with papillomas from $p19^{Arf\ -/MSM}$ and $p19^{Arf\ FVB/MSM}$ (Figure. 12a-m). In addition, the expression pattern of E-cadherin was similar to K14 (Figure.13a-l). These results suggest that the $p19^{Arf\,MSM}$ allele inhibits the epithelial-mesenchymal transition (EMT), as well as papilloma development and malignant conversion.

4-6 The $p19^{Arf\ MSM}$ allele reduces proliferative cells in mouse skin after TPA treatment. To investigate the effects of the $p19^{Arf}$ allele on cell proliferation in mouse skin, we carried out immunohistochemical analysis with the cell proliferation marker Ki67. As a result, there was no difference in the number of Ki67-positive cells in $p19^{Arf\ FVB/-}$, $p19^{Arf\,-/MSM}$ or $p19^{Arf\,FVB/MSM}$ mice in the absence of TPA (Figure. 14a, c, e, g). On the other hand, papillomas from $p19^{Arf\,FVB/-}$ mice had a significantly higher number of Ki67-positive cells compared with papillomas from $p19^{Arf\,-/MSM}$ and $p19^{Arf\,FVB/MSM}$ mice in the presence of TPA (Figure.14b, d, f, g). These results suggest that the $p19^{Arf\,MSM}$ allele more strongly suppresses cell proliferation in mouse skins after TPA treatment compared with the $p19^{Arf\,FVB}$ allele.

4-7 The genetic polymorphisms in *p19^{Arf}* differ in biological activity. To examine the function of the genetic polymorphisms in *p19^{Arf}*, we used mouse skins of *p19$^{Arf\ FVB/-}$*, *p19$^{Arf\ -/MSM}$* and *p19$^{Arf\ FVB/MSM}$*, as well as NIH/3T3 cells overexpressing *p19$^{Arf\ MSM}$* or *p19$^{Arf\ FVB}$*. We originally attempted to generate a mouse keratinocyte cell line (C5N) and carcinoma cell lines (B9, D3) that overexpressed *p19^{Arf}*. However, we were unable to generate cells overexpressing *p19^{Arf}*, probably because endogenous *p19^{Arf}* was highly expressed in these cell lines (C5N, B9, D3). Therefore, we used NIH/3T3 cells in which endogenous *p19^{Arf}* was nearly silenced[49]. NIH/3T3 cells were successfully transduced with retroviral vectors expressing *p19$^{Arf\ MSM}$*-HA or *p19$^{Arf\ FVB}$*-HA (Figure. 15a). These cells exhibited no difference in mRNA or protein expression levels between *p19^{ArfMSM}*-HA and *p19$^{Arf\ FVB}$*-HA (Figure. 15b-d).

As we observed an effect of the *p19^{Arf}* allele on cell proliferation in mouse skin (Fig. 14), we performed cell cycle analysis using skins of *p19$^{Arf\ FVB/-}$*, *p19$^{Arf\ -/MSM}$* and *p19$^{Arf\ FVB/MSM}$* mice, as well as NIH/3T3 cells overexpressing *p19$^{Arf\ MSM}$* or *p19$^{Arf\ FVB}$*. We observed subtle effects on cell cycle progression in untreated mouse skins and NIH/3T3 cells overexpressing *p19$^{Arf\ MSM}$* or *p19$^{Arf\ FVB}$* after DMSO treatment (Figure. 16a, b). On the other hand, the percentage of cells in G_0/G_1 phase was significantly lower in skin of *p19$^{Arf\ FVB/-}$* mice than in skin of *p19$^{Arf\ -/MSM}$* mice after TPA treatment (Figure. 16a).

Similarly, the percentage of NIH/3T3 cells overexpressing *p19*$^{Arf\ FVB}$ in G_0/G_1 phase was significantly lower than that of *p19*$^{Arf\ MSM}$-overexpressing cells after TPA treatment (Figure. 16b). In addition, the percentage of cells in S phase was significantly higher in skin of *p19*$^{Arf\ FVB/-}$ mice than in skin of *p19*$^{Arf\ -/MSM}$ mice after TPA treatment (Figure. 16a). Similarly, the percentage of NIH/3T3 cells overexpressing *p19*$^{Arf\ FVB}$ in S phase was significantly higher than that of *p19*$^{Arf\ MSM}$-overexpressing cells after TPA treatment (Figure. 16b). These results are consistent with Figure. 14, and suggest that the *p19*$^{Arf\ MSM}$ allele suppresses cell proliferation in normal cells by inducing G_1 arrest after TPA treatment.

Furthermore, we analyzed the p19^{Arf} expression level by Western blotting, and found that p19^{Arf} expression levels were increased by TPA treatment. In addition, p19^{Arf} expression was significantly higher in skin of *p19*$^{Arf\ -/MSM}$ mice than in skin of *p19*$^{Arf\ FVB/-}$ mice two days after TPA treatment (Figure. 16c, d). Similarly, p19^{Arf} expression was significantly higher in NIH/3T3 cells overexpressing *p19*$^{Arf\ MSM}$ than in *p19*$^{Arf\ FVB}$-overexpressing cells after TPA treatment (Figure. 16e, f). As *p19*$^{Arf\ MSM}$ *and p19*$^{Arf\ FVB}$ are expressed under the same promoter in NIH/3T3 cells, it is unlikely that these two proteins differ in quantity. A previous report suggested that TPA mediates the stabilization of p19^{Arf} [50], thus it is likely that p19$^{Arf\ MSM}$ is more stable than p19$^{Arf\ FVB}$.

4-8 Subcellular localization of p19^{Arf} is altered by TPA treatment. TPA was previously reported to upregulate Arf in the cytoplasm[50, 51]. *p19^{Arf}* mutants lacking the C-terminus were consistently expressed at lower levels compared with wild-type p19^{Arf}. A region encoded by exon 2 helps to stabilize the protein[52]. Therefore, we generated NIH/3T3 cells overexpressing *p19^{Arf}* mutants lacking the C-terminal region where the SNP is located (*⊿133-169*) and checked subcellular localization by immunostaining. As a results, *p19^{Arf}* mutants (*⊿133-169*) localized in the cytoplasm (Figure.17a-c). This result suggested that C-terminus of *p19^{Arf}* is involved in protein localization.

Next, we carried out immunostaining using NIH/3T3 cells overexpressing p19$^{Arf\ FVB}$ or p19$^{Arf\ MSM}$. We noted that p19$^{Arf\ MSM}$ was preferentially localized in the nucleus after TPA treatment. In contrast, p19$^{Arf\ FVB}$ was preferentially localized in the cytoplasm after TPA treatment (Figure. 18a-p). Furthermore, p19^{Arf} localization was confirmed by Western blot analysis using cytoplasmic and nuclear extracts. Efficient fractionation was confirmed by anti-α-Tubulin antibody for the cytoplasm and anti-Histone H3 antibody for the nucleus, as these proteins are mainly enriched in these cellular compartments. Fractionation experiments demonstrated that p19$^{Arf\ FVB}$ was more highly enriched in the cytoplasm compared with p19$^{Arf\ MSM}$ after TPA treatment (Figure. 18q, r). It has been

reported that Mdm2 mediates Arf degradation via proteasomes in the cytoplasm[51]. Accordingly, we evaluated the protein-protein interaction between ARF and Mdm2 in the cytoplasm and nucleus. $p19^{Arf\ MSM}$ was pulled-down significantly more than $p19^{Arf\ FVB}$ with Mdm2 in the nuclear extracts after TPA treatment (Figure. 19a, b). On the other hand, $p19^{Arf\ FVB}$ was pulled-down significantly more than $p19^{Arf\ MSM}$ with Mdm2 in the cytoplasmic extracts after TPA treatment (Figure. 19a, b). These results suggest that $p19^{Arf\ MSM}$ is mainly localized with Mdm2 in the nucleus and $p19^{Arf\ FVB}$ is mainly localized with Mdm2 in the cytoplasm. As Mdm2 mediates Arf degradation in the cytoplasm[46], $p19^{Arf\ FVB}$ may be more easily degraded compared with $p19^{Arf\ MSM}$, being a possible explanation for why $p19^{Arf\ MSM}$ is more stable than $p19^{Arf\ FVB}$ (Figure. 16 c-f).

4-9 $p19^{Arf\ MSM}$ activates the p53 pathway. $p19^{Arf}$ stabilizes p53 protein by inactivating Mdm2 protein to mediate p53 transactivation[49]. In addition, nuclear localization of p53 is necessary for this transactivation function[53, 54]. In this study, we found that $p19^{Arf\ MSM}$ is mainly localized with Mdm2 in the nucleus. Therefore, we investigated whether $p19^{Arf\ MSM}$ activates the p53 pathway more efficiently than $p19^{Arf\ FVB}$. First, we analyzed p53 expression levels in skins of $p19^{Arf\ -/MSM}$ and $p19^{Arf\ FVB/-}$ mice by Western blotting. As a result, p53 expression was significantly higher in skin of $p19^{Arf\ -/MSM}$ mice than in

skin of $p19^{Arf\ FVB/-}$ mice two days after TPA treatment (Figure. 20a, b). Similarly, p53 expression was significantly higher in NIH/3T3 cells overexpressing $p19^{Arf\ MSM}$ than in $p19^{Arf\ FVB}$-overexpressing cells after TPA treatment (Figure. 20c, d). Next, we measured mRNA expression levels of the p53 target genes *p21*, *Noxa* and *Bax*. p53 target gene expression was significantly higher in $p19^{Arf\ -/MSM}$ mice than in $p19^{Arf\ FVB/-}$ mice two days after TPA treatment (Figure. 20e). Similarly, p53 target gene expression was significantly higher in NIH/3T3 cells overexpressing $p19^{Arf\ MSM}$ than in $p19^{Arf\ FVB}$-overexpressing cells after TPA treatment (Figure. 20f). As increased p53 target gene expression strongly suggests the activation of p53[55-57], these data indicate that $p19^{Arf\ MSM}$ more efficiently induces the transcriptional activity of p53 compared with $p19^{Arf\ FVB}$.

4-10 Polymorphisms in *CDKN2A* are associated with human cancer risk. As a genetic variation in exon 2 of *Cdkn2a*/$p19^{Arf}$ was demonstrated to modify tumorigenesis in mice, we hypothesized that genetic variations in *CDKN2A* can influence carcinogenesis in humans. To investigate whether the human *CDKN2A* gene is associated with the incidence of cancer, we examined a large scale GWAS panel using approximately ten thousand Japanese cancer patients. Five SNPs in *CDKN2A* loci were

genotyped by Illumina Human Hap610 BeadChip using DNA from breast, colorectal, lung, prostate, liver, and gastric cancer patients. As the result, three SNP markers (rs2811708, rs3731217, rs3731239) located near the *CDKN2A* gene were found to be associated with the incidence of breast cancer (Table 3, Figure. 21). Among them, rs2811708 and rs3731217 exhibited a significant association even after Bonferroni correction ($P < 0.05/30$). All of these SNPs are located within introns (Figure. 21). Although the molecular mechanisms of these SNPs conferring susceptibility to cancers are unknown, *CDKN2A* SNPs may be associated with human cancer risk, like mice.

5. Discussion

In this study, we demonstrated that *Cdkn2a*/*p19*^{Arf} is one of the responsible genes for the *Stmm3* locus. Our skin carcinogenesis experiments revealed that the *p19*$^{Arf\ MSM}$ allele suppresses papilloma development and growth by reducing proliferative cells and malignant conversion. In addition, degradation stable p19$^{Arf\ MSM}$ protein is preferentially localized in the nucleus, which activates the p53 pathway.

These findings are partly consistent with our hypothesis. First, our congenic study suggested that the function of *Stmm3* is dependent on p53. The *Cdkn2a* locus encodes two major tumor suppressor genes, *p16*^{Ink4a} and *p19*^{Arf}, which enhance the growth-suppressive functions of pRb and the p53 protein, respectively[30-31]. It has been reported that there is a regulatory feedback circuit between p53 and p16^{Ink4a}, and the p16^{Ink4a} pathway is accelerated if *p53* is deleted, indicating a backup tumor suppressor role for *p16*^{Ink4a} after *p53* inactivation[58, 59]. In contrast, the function of *p19*^{Arf} is dependent on *p53*[58]. This is consistent with the results of our original linkage and congenic study. Second, previous reports suggested that *p19*^{Arf} regulates papilloma development, growth and malignant conversion[60]. However, *p16*^{Ink4a} did not regulate papilloma development or growth, and instead regulated malignant conversion according to another report[61]. Our congenic study suggested that *Stmm3* regulates

papilloma development, growth and malignant conversion. These results are consistent with the previous reports on *p19*^{Arf} and *p16*^{Ink4a}. Third, our animal experiments demonstrated that *p19*$^{Arf\,\mathrm{MSM}}$ confers stronger resistance to papillomas than *p16*$^{Ink4a\,\mathrm{MSM}}$ *in vivo*. Fourth, *p19*$^{Arf\,\mathrm{MSM}}$ is preferentially localized in the nucleus and activates the p53 pathway, clarifying that the function of *p19*$^{Arf\,\mathrm{MSM}}$ is dependent on *p53*. Taken together, we conclude that *p19*^{Arf} and not *p16*^{Ink4a} is a major responsible gene for *Stmm3*.

ARF is involved in the oncogenic checkpoint by sensitizing incipient cancer cells to growth arrest. This phenomenon is generally accompanied by parallel disruption of the inhibitory interaction between Mdm2 and p53[62, 63]. The *Cdkn2a*/*p19*^{Arf} locus is frequently deleted in human tumors, particularly in melanomas and pancreatic adenocarcinomas[64]. The N-terminal region of the human and mouse ARF proteins is necessary and sufficient for this function[65-67]. The stability and nucleolar sequestration of p19^{Arf} depends on its interaction with nucleophosmin (NPM), and the ability of p19^{Arf} to bind either Mdm2 or NPM is determined by N-terminal amino acid residues encoded by exon1β[68-70]. A small polypeptide specified by exon1β alone is capable of interacting with NPM and Mdm2, inducing acute p53-dependent cell cycle arrest[51, 65, 66]. It has been reported that non-nucleolar forms of ARF are subjected to rapid degradation by

proteasomes, with MDM2 playing a role in the modulation of this phenomenon[69, 70]. On the other hand, the human $p14^{ARF}$ mutation lacking the C-terminus (exon 2: 65-132 aa) does not affect the biological activity[65-68]. However, a genetic polymorphism which exists in the C-terminal region of $p19^{Arf}$ between MSM/Ms (Val) and FVB/N (Leu) was found to stabilize the protein and cause the protein to be localized in the nucleus. Arf was reported to be degraded, at least in part, by proteasomes in the cytoplasm[50]. Therefore, nuclear localization of $p19^{Arf}$ likely leads to stabilization of the protein. Indeed, human ARF lacks the C-terminal region where the SNP is located. As many studies have been performed using human ARF sequences, the biological importance of the C-terminal region may have been missed. Although the molecular mechanism of the C-terminus of $p19^{Arf}$ is unclear, ligating the mouse C-terminal region with human ARF may be an important experiment in the near future.

Furthermore, we clarified three novel SNPs in *CDKN2A* that are associated with the incidence of breast and lung cancer in the Japanese population. All of these SNPs are located in introns. However, the molecular mechanisms of these SNPs conferring susceptibility to cancers remain unknown. These SNPs may affect splicing or the expression of $p14^{ARF}$. Genotyping and expression analyses using human lymphoblastoid cell lines may be required for further studies as to whether *CDKN2A* SNPs are

associated with human cancer risk, as in mice.

In conclusion, we have demonstrated the cyclin-dependent kinase inhibitor gene *p19*^{Arf} to be a major responsible gene for the *Stmm3* locus. In addition, we found that a genetic polymorphism in *p19*^{Arf} between MSM/Ms (Val) and FVB/N (Leu) can modify susceptibility to skin carcinogenesis. Moreover, the *p19*$^{Arf\ MSM}$ allele more efficiently activates the p53 pathway compared with the *p19*$^{Arf\ FVB}$ allele *in vitro* and *in vivo*. Furthermore, we clarified novel polymorphisms in *CDKN2A*, which are in the vicinity of a polymorphism in mouse *Cdkn2a*, to be associated with the risk of human cancers in the Japanese population. Genetic polymorphisms in *Cdkn2a* and *CDKN2A* may modulate cancer risk in both mice and humans. Our data confirm that genetic approaches using mouse models can be translated to humans in order to identify cancer susceptibility alleles and molecular target therapies.

6. Acknowledgements

The author is especially grateful to Dr. Wakabayashi, Dr. Okumura, Dr. Isogai and Dr. Nagase for experimental planning and helpful discussion. The author thanks members of Laboratory of Experimental Animals for their kind supports. The author also thanks all members of Chiba Cancer Research Institute for their thoughtful provocative discussions during these projects.

This work was supported by JSPS KAKENHI Grant number 17J01656 and JP16H06276.

7. References

1. Balmain A. Cancer as a complex genetic trait: tumor susceptibility in humans and mouse models. *Cell*. **108**, 145-152 (2002).

2. Li FP *et al*. Identification and management of inherited cancer susceptibility. *Environ Health Perspect.* **103**, 297–300 (1995).

3. Houlston RS *et al*. The search for low-penetrance cancer susceptibility alleles. *Oncogene.* **23**, 6471–6476 (2004).

4. Stadler Z. K. *et al*. Genome-wide association studies of cancer. *J Clin Oncol*. **28**, 4255–4267 (2010).

5. Pérez-Losada J *et al*. Cancer evolution and individual susceptibility. *Integrative Biology.* **3**, 316–328 (2011).

6. Manolio T. A. *et al*. Finding the missing heritability of complex diseases. *Nature.* **461**, 747–753 (2009).

7. Tanikawa C et al. GWAS identifies two novel colorectal cancer loci at 16q24.1 and 20q13.12. *Carcinogenesis.* (2018).

8. Ashman LK *et al*. Two-stage skin carcinogenesis in sensitive and resistant mouse strains. *Carcinogenesis*. **3**, 99-102 (1982).

9. Bangrazi C *et al*. Genetics of chemical carcinogenesis. 1. Bidirectional selective breeding of susceptible and resistant lines of mice to two-stage skin carcinogenesis. *Carcinogenesis.* **11**, 1711-1719 (1990).

10. Nagase H *et al*. A subset of skin tumor modifier loci determines survival time of tumor-bearing mice. *Proc Natl Acad Sci U.S.A.* **96**, 15032–15037 (1999).

11. Nagase H *et al*. Distinct genetic loci control development of benign and malignant skin tumours in mice. *Nat Genet*. **10**, 424–429 (1995).

12. Fujiwara K *et al*. New chemically induced skin tumour susceptibility loci identified in a mouse backcross between FVB and dominant resistant PWK. *BMC Genet.* **8**, 39 (2007).

13. Fujiwara K *et al*. New outbred colony derived from Mus musculus castaneus to identify skin tumor susceptibility loci. *Mol. Carcinog*. **49**, 653–661 (2010).

14. Okumura K *et al*. Independent genetic control of early and late stages of chemically induced skin tumors in a cross of a Japanese wild-derived inbred mouse strain, MSM/Ms. *Carcinogenesis.* **33**, 2260–2268 (2012).

15. To M. D. *et al*. A functional switch from lung cancer resistance to susceptibility at the Pas1 locus in Kras2LA2 mice. *Nat Genet.* **38**, 926–930 (2006).

16. Santos J. *et al*. A new locus for resistance to gamma-radiation-induced thymic

lymphoma identified using inter-specific consomic and inter-specific recombinant congenic strains of mice. *Oncogene*. **21**, 6680–6683 (2002).

17. Peissel B. *et al.* Linkage disequilibrium and haplotype mapping of a skin cancer susceptibility locus in outbred mice. *Mamm Genome*. **11**, 979–981 (2000).

18. Wakabayashi Y. *et al*. Promotion of Hras-induced squamous carcinomas by a polymorphic variant of the Patched gene in FVB mouse. *Nature.* **445**, 761–765 (2007).

19. Angel J. M *et al*. Association of a murine chromosome 9 locus (Psl1) with susceptibility to mouse skin tumour promotion by 12-O-tetradecanoylphorbol-13-acetate. *Mol Carcinog*. **20**, 162–167 (1997).

20. Angel J. M et al. Identification of novel genetic loci contributing to 12-O-tetradecanoylphorbol-13-acetate skin tumour promotion susceptibility in DBA/2 and C57BL/6 mice. *Cancer Res*. **63**, 2747–2751 (2003).

21. Ewart-Toland A. *et al*. Identification of Stk6/STK15 as a candidate low-penetrance tumour-susceptibility gene in mouse and human. *Nat Genet*. **34**, 403–412 (2003).

22. Ha NH *et al*. The Circadian Rhythm Gene Arntl2 Is a Metastasis Susceptibility Gene for Estrogen Receptor-Negative Breast Cancer. *PLoS Genet*. **12**, e1006267 (2016)

23. Kawasaki K *et al*. Genetic variants of Adam17 differentially regulate TGFβ

signaling to modify vascular pathology in mice and humans. *Proc Natl Acad Sci U S A*. **111**, 7723-7728 (2014)

24. Okumura K *et al*. Congenic mapping and allele-specific alteration analysis of Stmm1 locus conferring resistance to early-stage chemically induced skin papillomas. *PLoS One*. **20,** e97201 (2014).

25. Saito M *et al*. Identification of *Stmm3* locus conferring resistance to late-stage chemically induced skin papillomas on mouse chromosome 4 by congenic mapping and allele-specific alteration analysis. *Exp Anim.* **63**, 339-348 (2014).

26. Okumura K et al. The parathyroid hormone regulates skin tumour susceptibility in mice. *Sci Rep*. **7**, 11208 (2017)

27. Zhang S *et al*. Cdkn2a, the cyclin-dependent kinase inhibitor encoding p16INK4a and p19ARF, is a candidate for the plasmacytoma susceptibility locus, Pctr1. *Proc. Natl. Acad. Sci. U. S. A.* **95**, 2429-34 (1998).

28. Zhang SL *et al*. Efficiency alleles of the Pctr1 modifier locus for plasmacytoma susceptibility. *Mol Cell Biol*. **21**, 310-318 (2001).

29. Zhang Z *et al*. A strong candidate gene for the Papg1 locus on mouse chromosome 4 affecting lung tumor progression. *Oncogene*. **21**, 5960-5966 (2002).

30. Carnero A et al. p16INK4A and p19ARF act in overlapping pathways in cellular

immortalization. *Nat Cell Biol*. **2**, 148-155 (2000)

31. Serrano M. The INK4a/ARF locus in murine tumorigenesis. *Carcinogenesis*. **21**, 865-869 (2000)

32. Song X *et al*. Potentially functional variants of p14ARF are associated with HPV-positive oropharyngeal cancer patients and survival after definitive chemoradiotherapy. *Carcinogenesis*. **35**, 62-68 (2014).

33. Migliorini G *et al*. Variation at 10p12.2 and 10p14 influences risk of childhood B-cell acute lymphoblastic leukemia and phenotype. *Blood*. **122**, 3298-3307 (2013).

34. Zhang F *et al*. Significance of MDM2 and P14 ARF polymorphisms in susceptibility to differentiated thyroid carcinoma. *Surgery*. **153**, 711-717 (2013).

35. Zhang Y *et al*. p14ARF genetic polymorphisms and susceptibility to second primary malignancy in patients with index squamous cell carcinoma of the head and neck. *Cancer*. **117**, 1227-1235 (2011).

36. Sherborne AL *et al*. Variation in CDKN2A at 9p21.3 influences childhood acute lymphoblastic leukemia risk. *Nat Genet*. **42**, 492-494 (2010).

37. Vijayakrishnan J *et al*. Variation at 7p12.2 and 10q21.2 influences childhood acute lymphoblastic leukemia risk in the Thai population and may contribute to racial differences in leukemia incidence. *Leuk Lymphoma*. **51**, 1870-1874 (2010).

38. Driver KE *et al*. Association of single-nucleotide polymorphisms in the cell cycle genes with breast cancer in the British population. *Carcinogenesis*. **29**, 333-341 (2008).

39. Goode EL *et al*. Candidate gene analysis using imputed genotypes: cell cycle single-nucleotide polymorphisms and ovarian cancer risk. *Cancer Epidemiol Biomarkers Prev*. **18**, 935-944 (2009).

40. Gu F *et al*. Common genetic variants in the 9p21 region and their associations with multiple tumours. *Br J Cancer*. **108**, 1378-1386 (2013).

41. Li WQ *et al*. Genetic polymorphisms in the 9p21 region associated with risk of multiple cancers. *Carcinogenesis*. **35**, 2698-2705 (2014).

42. Araki K *et al*. Establishment of germline-competent embryonic stem cell lines from the MSM/Ms strain. *Mamm Genome*. **20**, 14-20 (2009).

43. Donehower LA *et al*. Mice deficient for p53 are developmentally normal but susceptible to spontaneous tumours. *Nature*. **356**, 215-221 (1992).

44. Kamijo T *et al*. Tumor suppression at the mouse INK4a locus mediated by the alternative reading frame product p19ARF. *Cell*. **91**, 649-659 (1997).

45. Sakurai T *et al*. Rapid zygosity determination in mice by SYBR Green real-time genomic PCR of a crude DNA solution. *Transgenic Res.* **17**, 149-155 (2008).

46. Lichti U *et al*. Isolation and short-term culture of primary keratinocytes, hair follicle populations and dermal cells from newborn mice and keratinocytes from adult mice for in vitro analysis and for grafting to immunodeficient mice. *Nat Protoc.* **3**, 799-810 (2008).

47. Kemp C.J. *et al*. Reduction of p53 gene dosage does not increase initiation or promotion but enhances malignant progression of chemically induced skin tumors. *Cell*. **74**, 813–822 (1993).

48. Tokarsky-Amiel R *et al*. Dynamics of senescent cell formation and retention revealed by p14ARF induction in the epidermis. *Cancer Res*. **73**, 2829-2839 (2013).

49. Kamijo T *et al*. Functional and physical interactions of the ARF tumor suppressor with p53 and Mdm2. *Proc. Natl. Acad. Sci. U.S.A.* **95**, 8292–8297 (1998).

50. Inoue R *et al*. PKCa is involved in phorbol ester TPA-mediated stabilization of p14ARF. *BBRC.* **330**, 1314-1318 (2005).

51. Vivo M *et al*. MDM2-Mediated Degradation of p14ARF: A Novel Mechanism to Control ARF Levels in Cancer Cells. *PLoS One*. **10**, e0117252 (2015).

52. Quelle DE *et al*. Cancer-associated mutations at the INK4a locus cancel cell cycle arrest by p16INK4a but not by the alternative reading frame protein p19ARF. *Proc*

Natl Acad Sci U S A. **92**, 669-673 (1997).

53. Gannon JV *et al*. Protein synthesis required to anchor a mutant p53 protein which is temperature-sensitive for nuclear transport. *Nature*. **349**, 802-806 (1991).

54. Shaulsky G *et al*. Nuclear localization is essential for the activity of p53 protein. *Oncogene*. **6**, 2055-2065 (1991).

55. Miyashita T *et al*. Tumor suppressor p53 is a direct transcriptional activator of the human bax gene. *Cell*. **80**, 293-299 (1995).

56. Oda E *et al*. Noxa, a BH3-only member of the Bcl-2 family and candidate mediator of p53-induced apoptosis. *Science*. **288**, 1053-1058 (2000).

57. Wagner AJ *et al*. Myc-mediated apoptosis requires wild-type p53 in a manner independent of cell cycle arrest and the ability of p53 to induce p21waf1/cip1. *Genes Dev*. **8**, 2817-2830 (1994).

58. Chazal M *et al*. P16(INK4A) is implicated in both the immediate and adaptative response of human keratinocytes to UVB irradiation. *Oncogene*. **21**, 2652-2661 (2002)

59. Smeets SJ *et al*. Immortalization of oral keratinocytes by functional inactivation of the p53 and pRb pathways. *Int J Cancer*. **128**, 1596-1605.

60. Kelly-Spratt KS *et al*. p19Arf suppresses growth, progression, and metastasis of

Hras-driven carcinomas through p53-dependent and -independent pathways. *PLoS Biol*. **2**, E242 (2004).

61. Takeuchi S *et al*. Intrinsic cooperation between p16INK4a and p21Waf1/Cip1 in the onset of cellular senescence and tumor suppression in vivo. *Cancer Res*. **70**, 9381-9390 (2010)

62. Brady CA et al. p53 at a glance. *J Cell Sci*. **123**, 2527–2532 (2010).

63. Zhang Y *et al*. Control of p53 ubiquitination and nuclear export by MDM2 and ARF. *Cell Growth Differ* **12**, 175–186 (2001).

64. Sharpless NE *et al.* The INK4A/ARF locus and its two gene products. *Curr Opin Genet Dev*. **9**, 22-30 (1999).

65. Weber JD *et al*., Cooperative signals governing ARF-mdm2 interaction and nucleolar localization of the complex. *Mol Cell Biol*. 20, 2517-2528 (2000).

66. DiGiammarino EL et al., Solution structure of the p53 regulatory domain of the p19Arf tumor suppressor protein. *Biochemistry*. **40**, 2379-2386 (2001).

67. Zhang Y *et al*. ARF promotes MDM2 degradation and stabilizes p53: ARF-INK4a locus deletion impairs both the Rb and p53 tumor suppression pathways. *Cell*. **92**, 725-734 (1998).

68. Vivo M *et al*. Mimicking p14ARF Phosphorylation Influences Its Ability to

Restrain Cell Proliferation. *PLoS One*. **8**, e53631 (2013).

69. Kuo ML *et al*. N-terminal polyubiquitination and degradation of the Arf tumor suppressor. *Genes Dev*. **18**, 1862–1874 (2004).

70. Rodway H *et al*. Stability of nucleolar versus non-nucleolar forms of human p14ARF. *Oncogene*. **23**, 6186–6192 (2004).

8. Figures and Tables

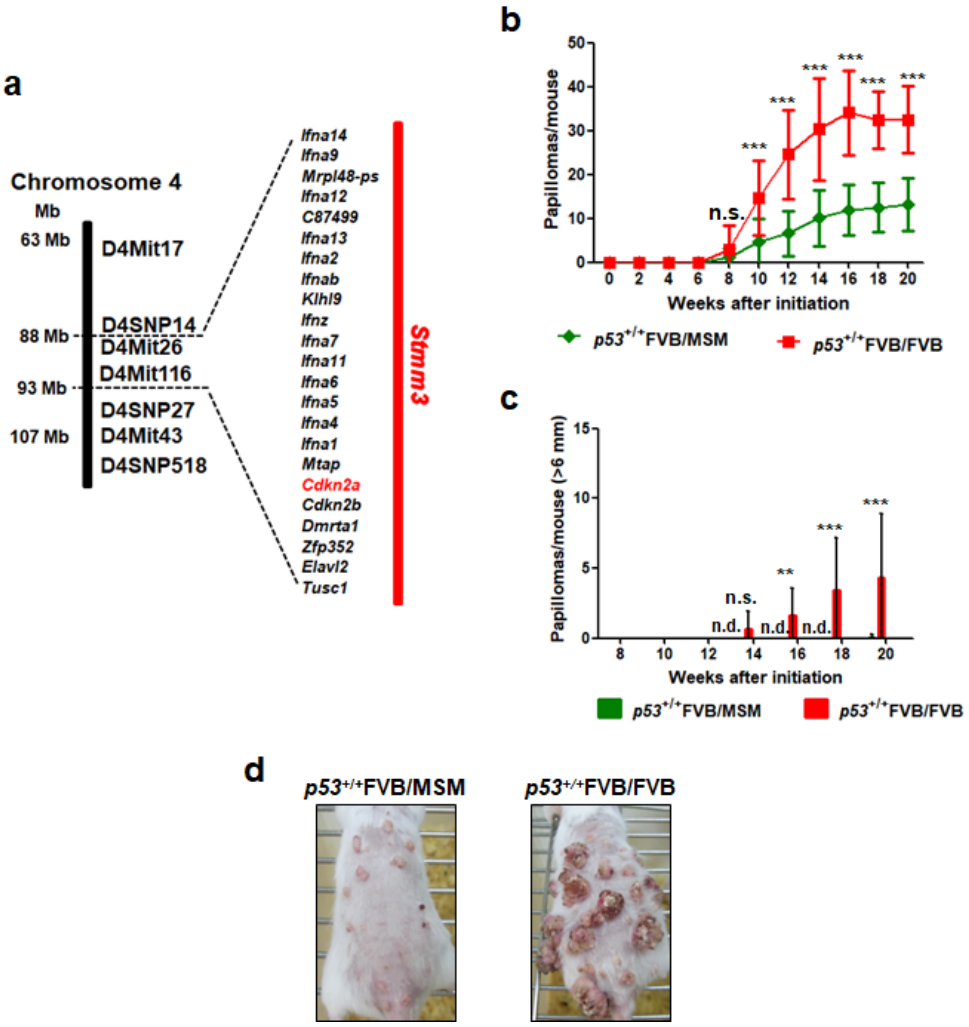

Figure 1. The *Stmm3* (Skin tumor modifier of MSM) locus controlling the transition to large papillomas on mouse chromosome 4. (a) A schematic representation of the genetic position around *Stmm3*. The red bar represents the region of *Stmm3*. Genetic positions shown are according to the Ensemble Database (http://www.ensembl.org/) and the Mouse Genome Informatics Database (http://www.informatics.jax.org/). (b) Comparison of average number of papillomas/mouse among $p53^{+/+}$F/M (n=17; 13.2±6.0), $p53^{+/+}$F/F mice (n=20; 32.5± 7.6). (c) Number of papillomas >6mm per mice in $p53^{+/+}$F/M, $p53^{+/+}$F/F mice (F/M: 0.059±0.24, F/F: 4.32±4.58). Number of papillomas is shown at 20 weeks after initiation. (d) Representative photographs of $p53^{+/+}$F/F congenic mice and $p53^{+/+}$F/M congenic mice at 20 weeks after initiation. n.d., not detected. The *P*-values were calculated by one-way ANOVA (***P<0.001, **P<0.01). n.s., not significant. Error bars represent the standard deviation (S.D.).

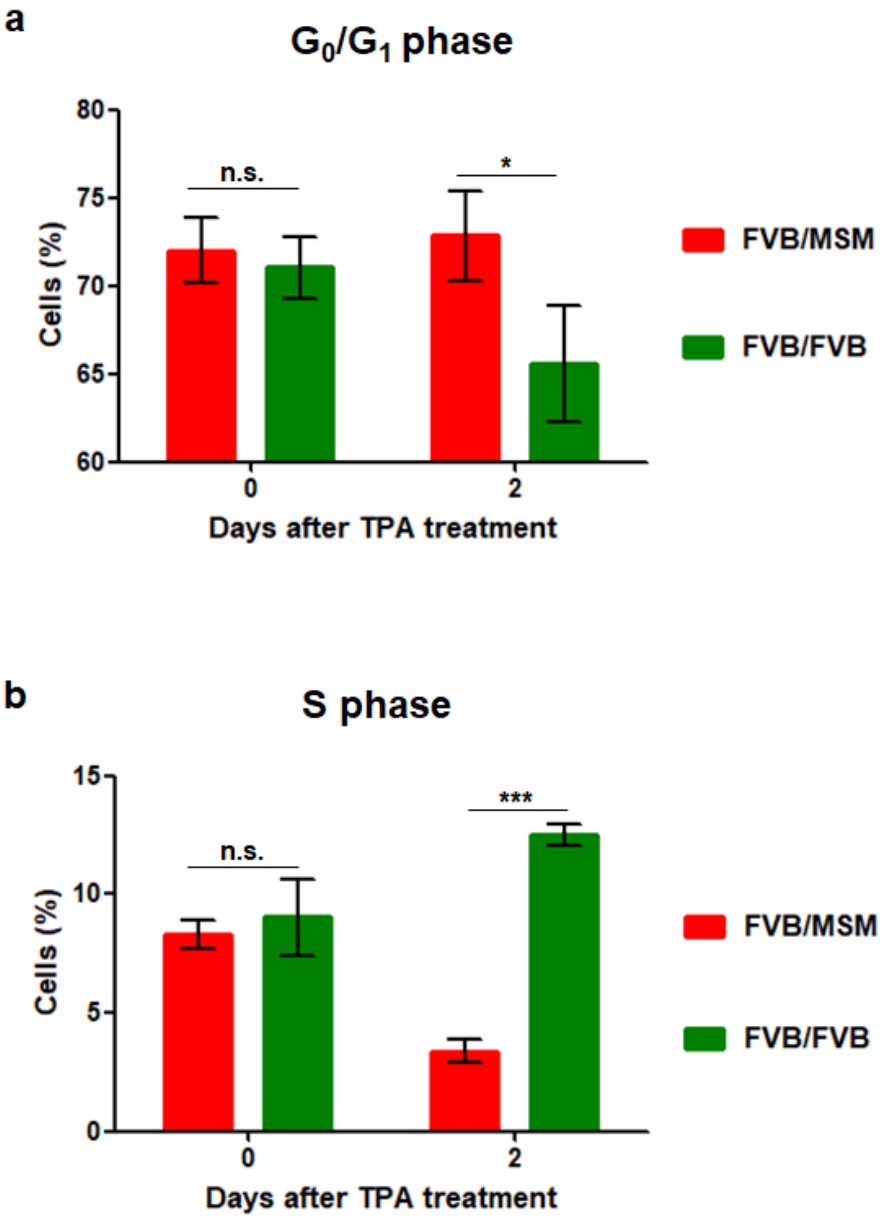

Figure 2. The *Stmm3* locus induces G_1 arrest following TPA treatment. (a-b) Cell cycle analysis of TPA-treated skin from *p53*$^{+/+}$F/M (n=3) (red bar) and *p53*$^{+/+}$F/F mice (n=3) (green bar) (0 day and 2 days after TPA treatment). (a) G_0/G_1 phase, (b) S phase. DNA content was measured by propidium iodide (PI) staining. The *P*-values were calculated by one-way ANOVA (***P*<0.01, **P*<0.05). n.s., not significant. Error bars represent the standard deviation (S.D.).

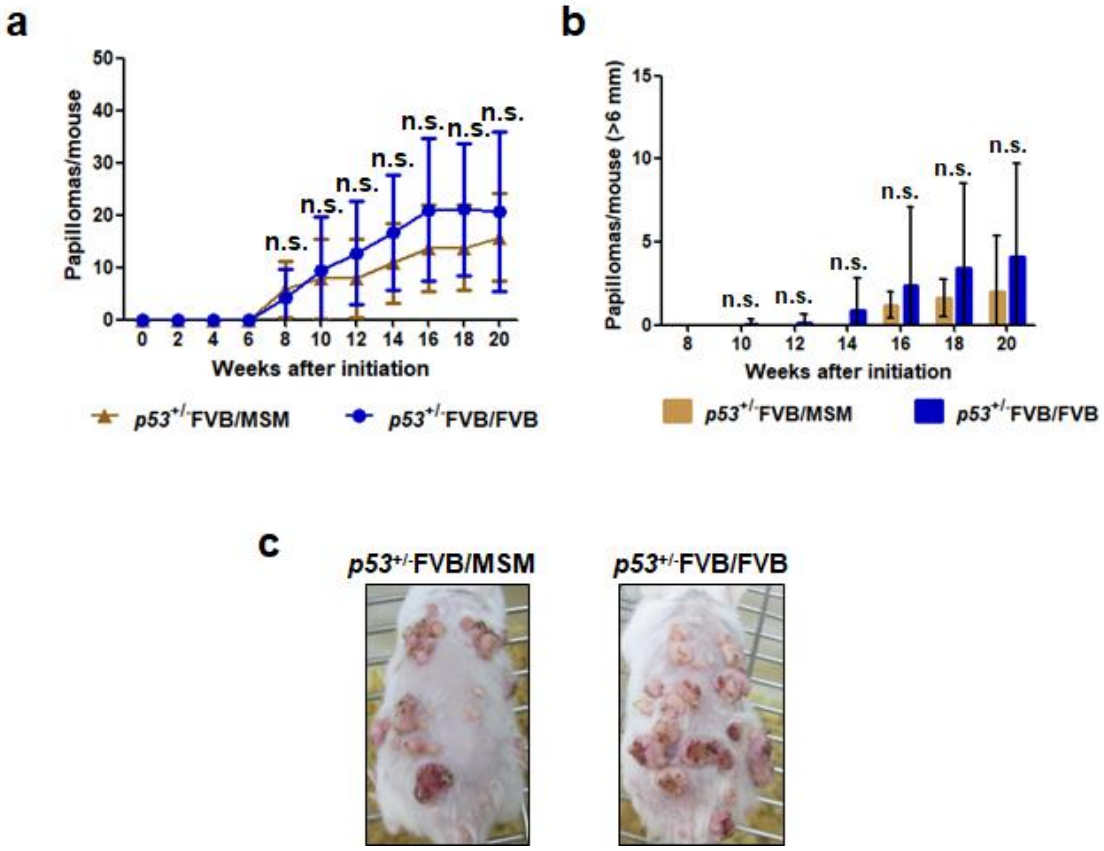

Figure 3. The effects of the *Stmm3* locus are dependent on *p53*. (a) Comparison of average number of papilllomas/mouse among *p53*$^{+/-}$F/M (n=15; 15.2±14.9) and *p53*$^{+/-}$F/F mice (n=15; 20.7±15.2). (b) Number of papillomas >6mm per mice in *p53*$^{+/-}$F/M, and *p53*$^{+/-}$F/F mice (F/M: 2.0±3.3, F/F: 4.2±5.7). Number of papillomas is shown at 20 weeks after initiation. (c) Representative photographs of *p53*$^{+/-}$F/F congenic mice and *p53*$^{+/-}$F/M congenic mice at 20 weeks after initiation. The *P*-values were calculated by one-way ANOVA. n.s., not significant. Error bars represent the standard deviation (S.D.).

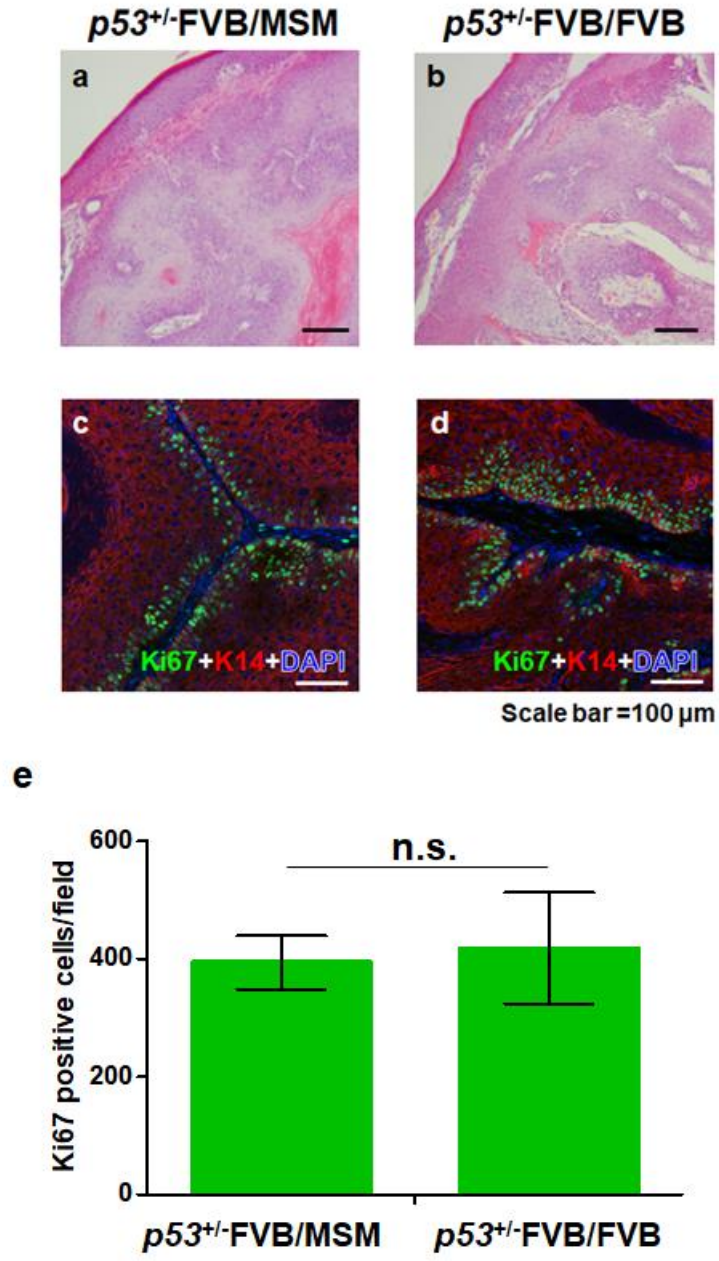

Figure 4. Papillomas from *p53*$^{+/-}$ sub-congenic mice have no differences in development. (a-b) HE staining patterns of papillomas from (a) *p53*$^{+/-}$F/M and (b) *p53*$^{+/-}$F/F. (c-d) Double-immunostaining patterns of Ki67 (green) and keratin 14 (K14) (red) in papillomas from (c) *p53*$^{+/-}$F/M and (d) *p53*$^{+/-}$F/F mice. Cells were counterstained with DAPI (blue). (e) The number of Ki67-positive cells in papillomas from *p53*$^{+/-}$F/M (n=14) and *p53*$^{+/-}$F/F mice (n=13). The *P*-value for the Ki67-positive cell number was calculated by one-way ANOVA (n.s., not significant.). Error bars represent the standard deviation (S.D.).

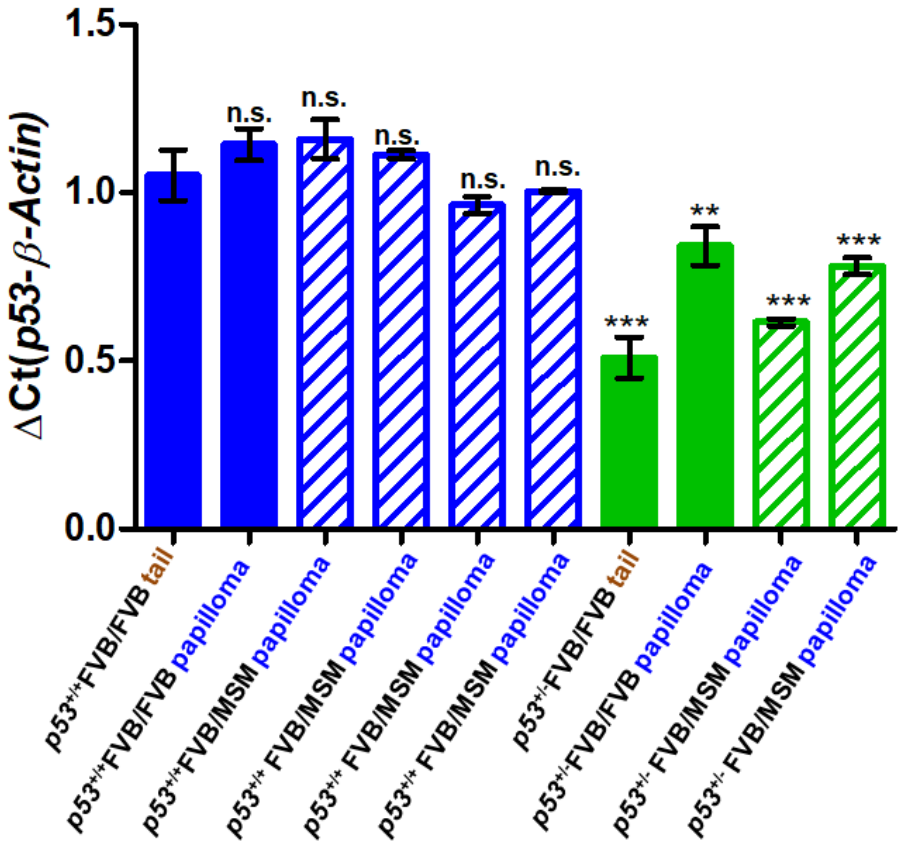

Figure 5. No difference between *p53*$^{+/+}$heterozygous congenic mice and *p53*$^{+/+}$homozygous congenic mice. ⊿Ct values (*p53* - *β-Actin*) were detected by SYBR Green real-time genomic PCR using papilloma DNA from *p53*$^{+/+}$ or *p53*$^{+/-}$ F/M mice (blue diagonal line bars and green diagonal line bars, respectively) and *p53*$^{+/+}$ or *p53*$^{+/-}$ F/F mice (blue bars and green bars, respectively). Tail samples were used as normal genomic DNA. All samples compared with *p53*$^{+/+}$F/F tail. The *P*-values were calculated by two-way ANOVA (***P<0.001, **P<0.01). n.s., not significant. Error bars represent the standard deviation (S.D.).

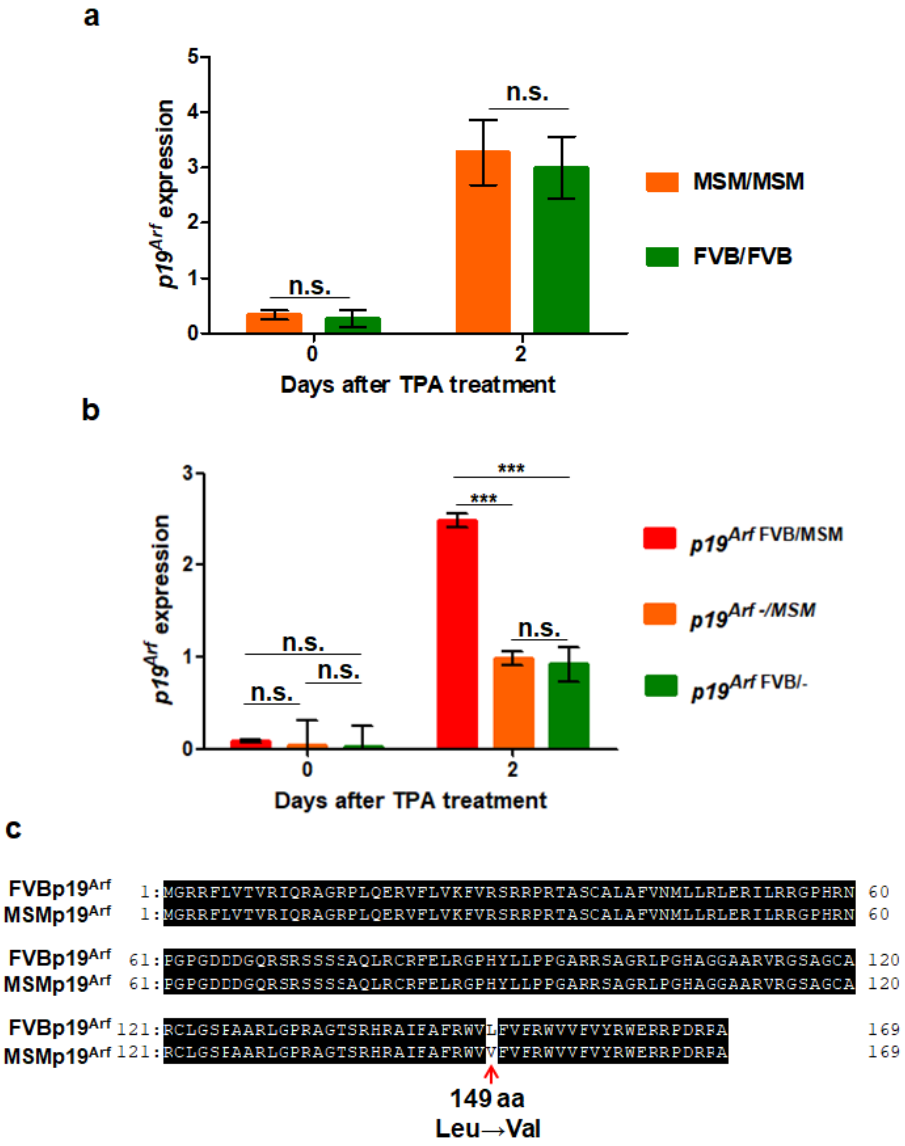

Figure 6. The *p19*^{Arf} expression levels in mouse skin and alignment of p19^{Arf} amino acid. (a) mRNA expression level of *p19*^{Arf}. qRT-PCR analysis of TPA-treated skins from M/M (MSM/MSM) (n=3) and F/F mice (FVB/FVB) (n=3) (0 and 2 days after TPA treatment). (b) qRT-PCR analysis of TPA-treated skins from *p19*$^{Arf\ FVB/MSM}$ (red bars), *p19*$^{Arf\ -/MSM}$ (orange bars), and *p19*$^{Arf\ FVB/-}$ (green bars) mice (n=3) (0 and 2 days after TPA treatment). The *P*-values were calculated by one- and two-way ANOVA (***P<0.001). n.s., not significant. Error bars represent the standard deviation (S.D.). (b) Alignment of p19^{Arf} of FVB/N and MSM/Ms. Red arrow indicates genetic variation between MSM/Ms (Val) and FVB/N (Leu).

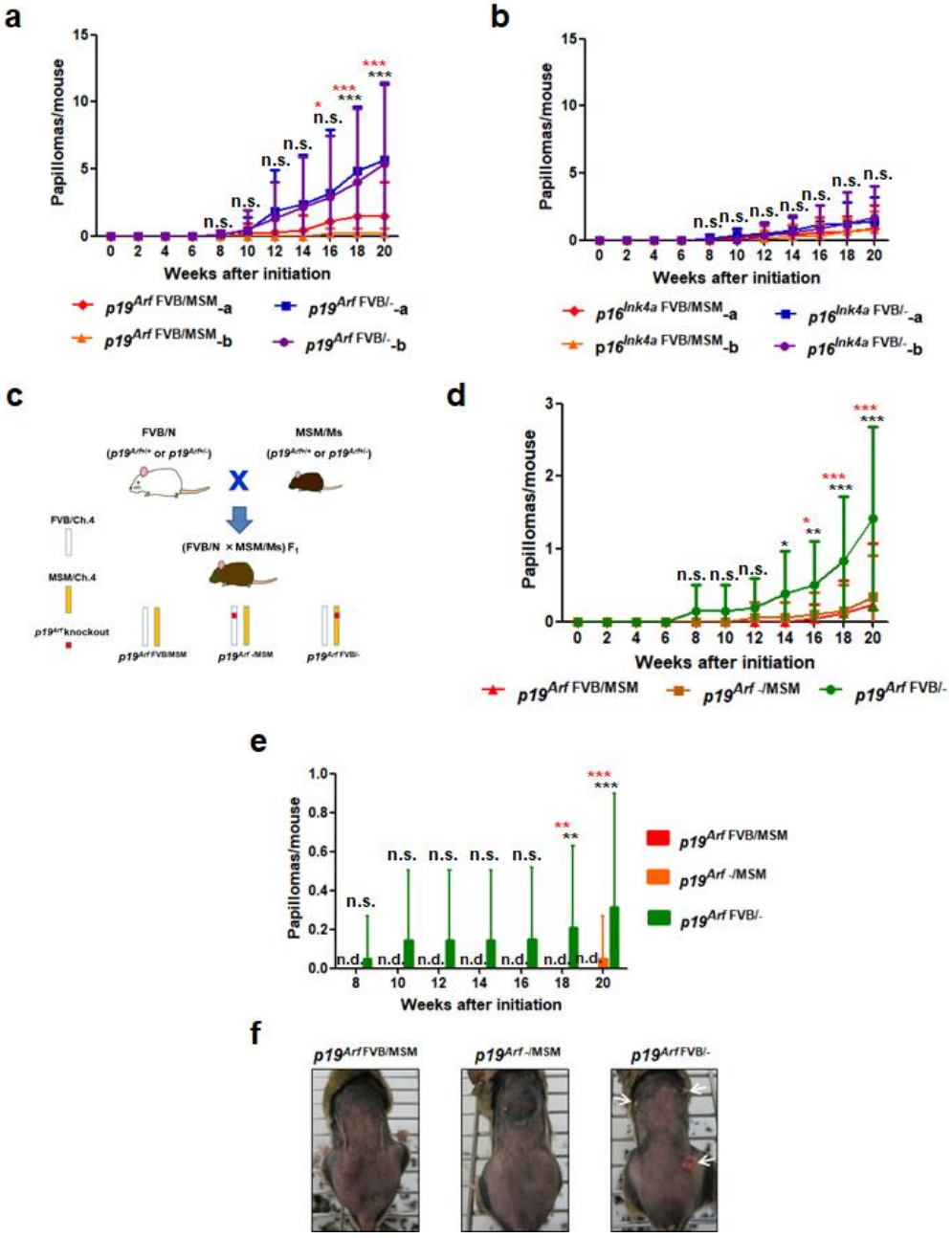

Figure 7. The *p19*$^{Arf\ MSM}$ allele confers resistance to larger papillomas. (a) Comparison of number of papillomas among *p19*$^{Arf\ FVB/MSM}$-a (n=11; 1.50±2.56), *p19*$^{Arf\ FVB/MSM}$-b (n=16: 0.18±0.40), *p19*$^{Arf\ FVB/-}$-a (n=17: 5.65±5.67) and *p19*$^{Arf\ FVB/-}$-b mice (n=17; 5.41±6.07). (b) Comparison of number of papillomas among *p16*$^{Ink4a\ FVB/MSM}$-a (n=16; 0.89±1.69), *p16*$^{Ink4a\ FVB/MSM}$-b (n=13: 0.77±1.36), *p16*$^{Ink4a\ FVB/-}$-a (n=21: 1.43±1.75) and *p16*$^{Ink4a\ FVB/-}$-b mice (n=19: 1.72±2.32). (c) A schematic drawing of the generation of *p19*$^{Arf+/-}$ (FVB/N×MSM/MS) F_1 mice. The orange bar indicates the MSM allele, whereas the white bar indicates the FVB allele. The red box indicates the *p19*^{Arf}

knockout allele. (d) Comparison of number of papillomas among $p19^{Arf\ FVB/MSM}$ (n=22: 0.52±0.47), $p19^{Arf\ -/MSM}$ (n=20: 0.52±0.80), and $p19^{Arf\ FVB/-}$ mice (n=21: 2.31±2.83). (e) Number of papillomas >6mm per mice in$p19^{Arf\ FVB/MSM}$ (not detected), $p19^{Arf\ -/MSM}$ (0.048±0.22), and $p19^{Arf\ FVB/-}$ mice (0.32±0.58). Number of papillomas is shown at 20 weeks after initiation. (f) Representative photographs of $p19^{Arf\ FVB/MSM}$ (left), $p19^{Arf\ -/MSM}$ (middle), and $p19^{Arf\ FVB/-}$ mouse (right) at 20 weeks after initiation. The white arrow indicates papillomas. (a) Red asterisks indicated $p19^{Arf\ FVB/MSM}$-a vs $p19^{Arf\ FVB/-}$-a. Black asterisks indicated $p19^{Arf\ FVB/MSM}$-b vs $p19^{Arf\ FVB/-}$-b. (d, e) Red asterisks indicated $p19^{Arf\ -/MSM}$ vs $p19^{Arf\ FVB/-}$. Black asterisks indicated $p19^{Arf\ FVB/MSM}$ vs $p19^{Arf\ FVB/-}$. n.d., not detected. The *P*-values were calculated by two-way ANOVA (***P<0.001, **P<0.01, *<0.05). n.s., not significant. Error bars represent the standard deviation (S.D.).

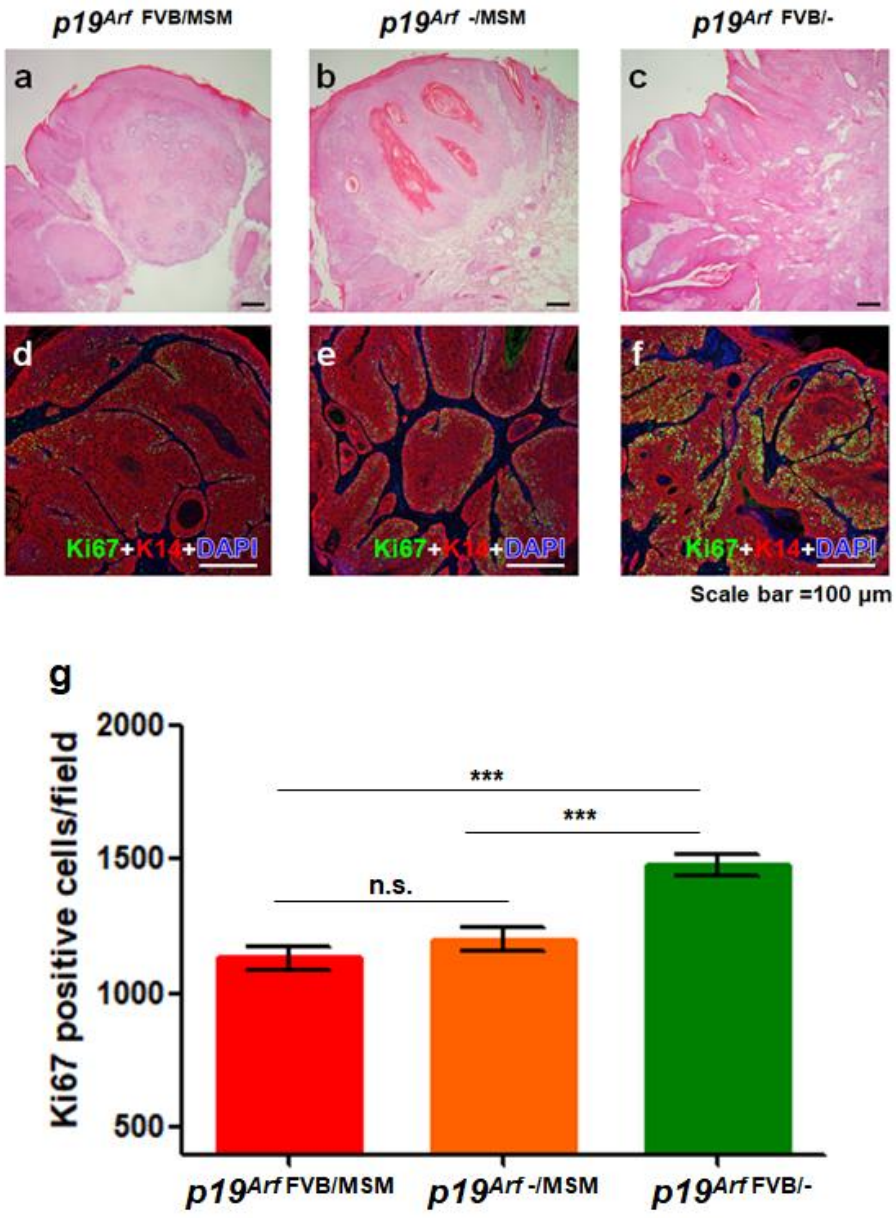

Figure 8. The *p19*$^{Arf\ MSM}$ allele regulates cell proliferation in papillomas. (a-c) HE staining patterns from a (a) *p19*$^{Arf\ FVB/MSM}$, (b) *p19*$^{Arf\ -/MSM}$, and (c) *p19*$^{Arf\ FVB/-}$ mouse. (d-f) Double-immunostaining patterns of Ki67 (green) and keratin 14 (K14) (red) in papillomas from a (d) *p19*$^{Arf\ FVB/MSM}$, (e) *p19*$^{Arf\ -/MSM}$, and (f) *p19*$^{Arf\ FVB/-}$ mouse. Cells were counterstained with DAPI (blue). (g) The number of Ki67-positive cells in papillomas from a *p19*$^{Arf\ FVB/MSM}$ (n=11) (red bars), *p19*$^{Arf\ -/MSM}$ (n=11) (orange bars), and *p19*$^{Arf\ FVB/-}$ mouse (n=11) (green bars). The *P*-value for number of Ki 67-positive cells was calculated by two-way ANOVA (***P<0.001). n.s., not significant. Error bars represent the standard deviation (S.D.).

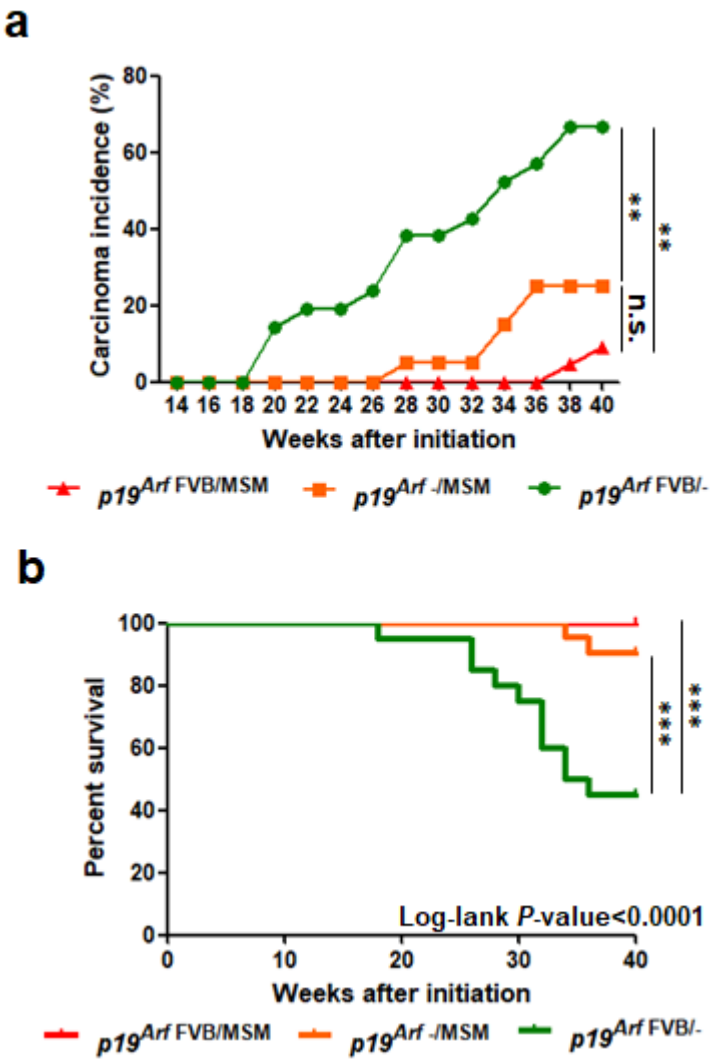

Figure 9. Malignant conversion differs between the *p19*$^{Arf\ MSM}$ allele and *p19*$^{Arf\ FVB}$ allele. (a) Comparison of DMBA/TPA-induced carcinoma incidence among *p19*$^{Arf\ FVB/MSM}$ (n=22: 9.1%), *p19*$^{Arf\ -/MSM}$ (n=20: 25.0%), and *p19*$^{Arf\ FVB/-}$ mice (n=21: 66.7%). Carcinoma incidences are shown at 40 weeks after initiation. (b) Survival curve of DMBA/TPA-treated *p19*$^{Arf\ FVB/MSM}$ (n=22), *p19*$^{Arf\ -/MSM}$ (n=20), and *p19*$^{Arf\ FVB/-}$ mice (n=21: median survival, 35weeks after initiation) (***P < 0.0001, Kaplan–Meier method). The P-values were calculated for carcinoma incidence at 40 weeks by Fisher's test (**P<0.01).

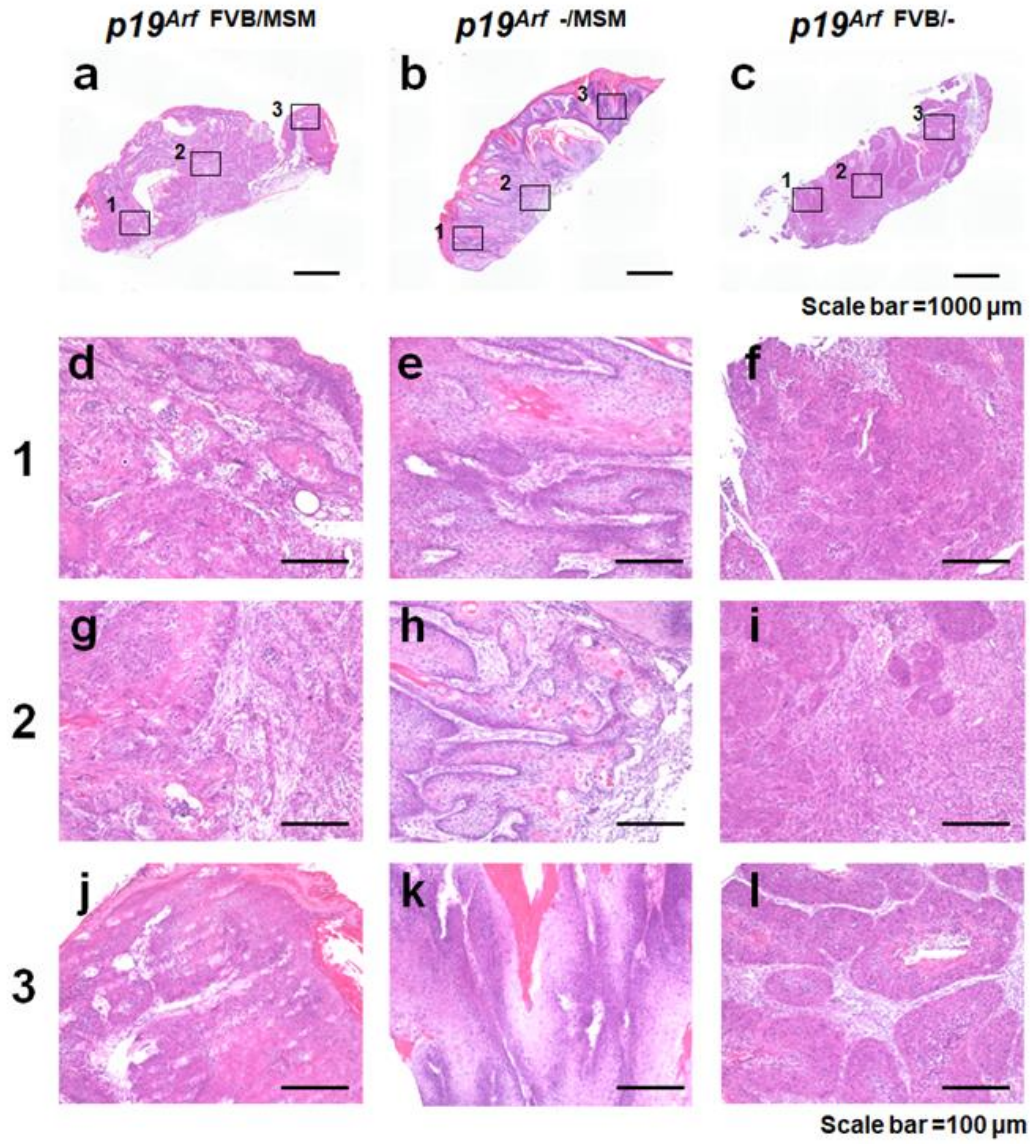

Figure 10. HE staining revealed no significant morphological changes. (a-l) HE staining patterns in carcinomas from *p19*$^{Arf\ FVB/MSM}$, *p19*$^{Arf\ -/MSM}$, and *p19*$^{Arf\ FVB/-}$ mice. (d-l) are magnified regions in white boxes in (a-c). Scale bars=1,000 μm (a-c), 100 μm (d-l).

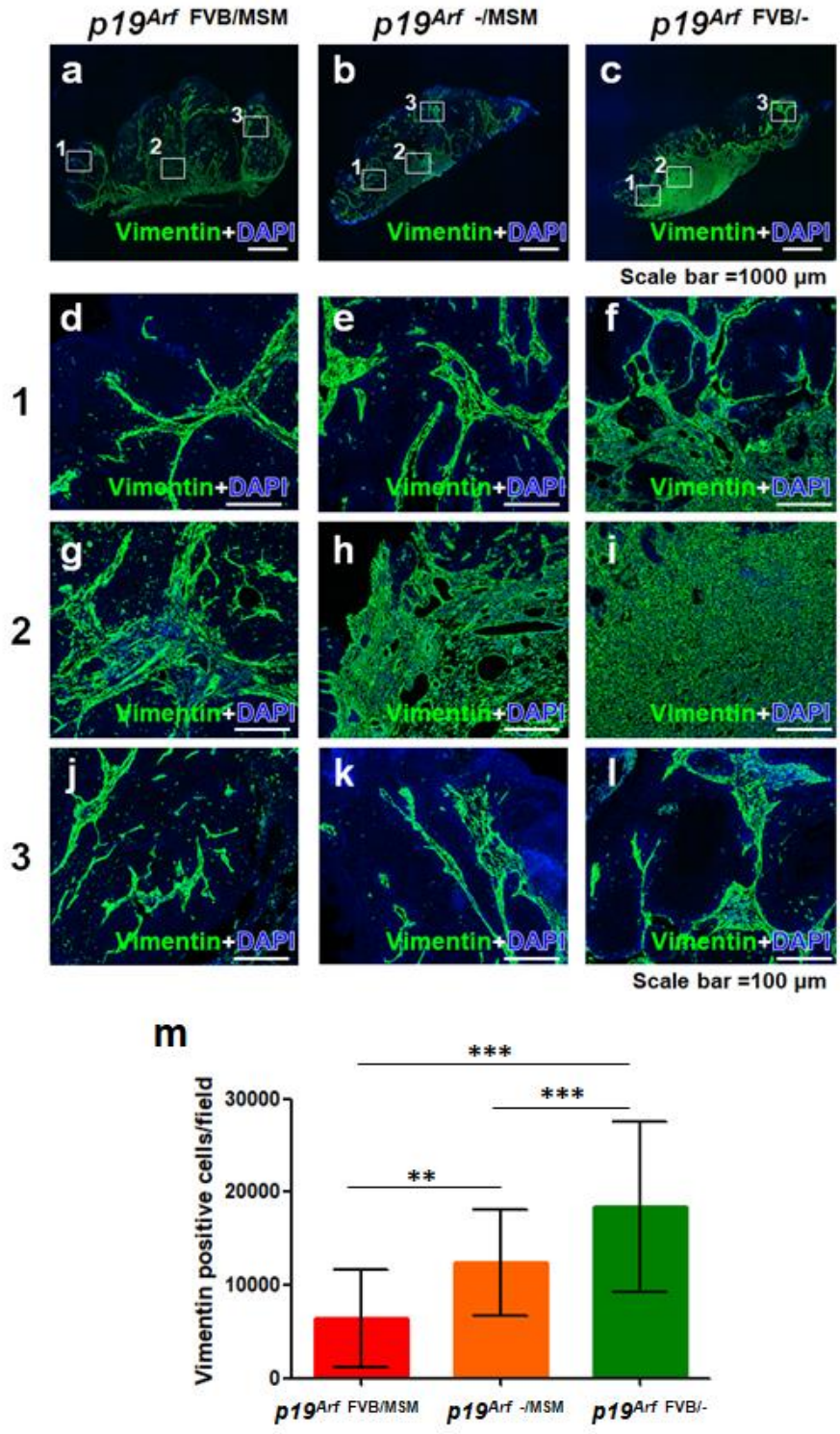

Figure 11. Immunostaining pattern of Vimentin in carcinomas. (a-l) Immunostaining pattern of vimentin (green) in carcinomas from *p19*$^{Arf\ FVB/MSM}$, *p19*$^{Arf\ -/MSM}$, and *p19*$^{Arf\ FVB/-}$ mice. (d-l) are magnified regions in white boxes in (a-c). Cells were counterstained with DAPI (blue). Scale bars=1,000 μm (a-c), 100 μm (d-l). (m)

The number of vimentin-positive cells in carcinomas from a $p19^{Arf\ FVB/MSM}$ (n=27) (red bars), $p19^{Arf\ -/MSM}$ mouse (n=43) (orange bars), and $p19^{Arf\ FVB/-}$ mice (n=46) (green bars). Vimentin-positive cells were calculated in magnified sections. The *P*-value for the vimentin-positive cell number was calculated by two-way ANOVA (***P<0.001, **P<0.01). Error bars represent the standard deviation (S.D.).

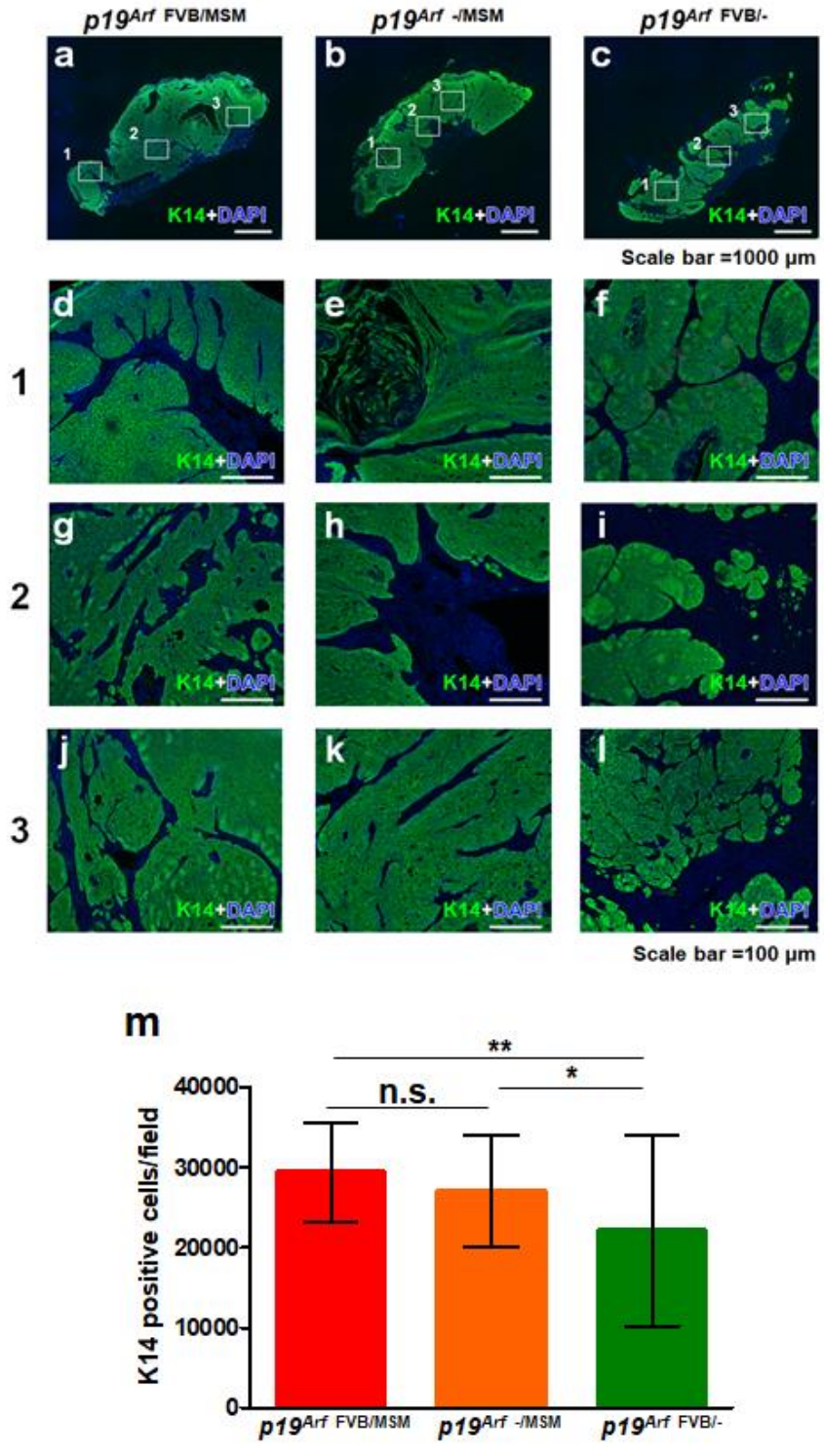

Figure 12. Immunostaining pattern of K14 in carcinomas. (a-l) Immunostaining patterns of K14 (green) in carcinomas from *p19*$^{Arf\ FVB/MSM}$, *p19*$^{Arf\ -/MSM}$, and *p19*$^{Arf\ FVB/-}$ mice. (d-l) are magnified regions in white boxes in (a-c). Cells were counterstained with DAPI (blue). Scale bars=1,000 μm (a-c), 100 μm (d-l). (m) The number of K14-positive

cells in carcinomas from a $p19^{Arf\ FVB/MSM}$ (n=27) (red bars), $p19^{Arf\ -/MSM}$ (n=43) (orange bars), and $p19^{Arf\ FVB/-}$ mouse (n=46) (green bars). K14-positive cells were counted in magnified sections. The *P*-value for number of K14-positive cells was calculated by two-way ANOVA (***P*<0.01, **P*<0.05). n.s., not significant. Error bars represent the standard deviation (S.D.).

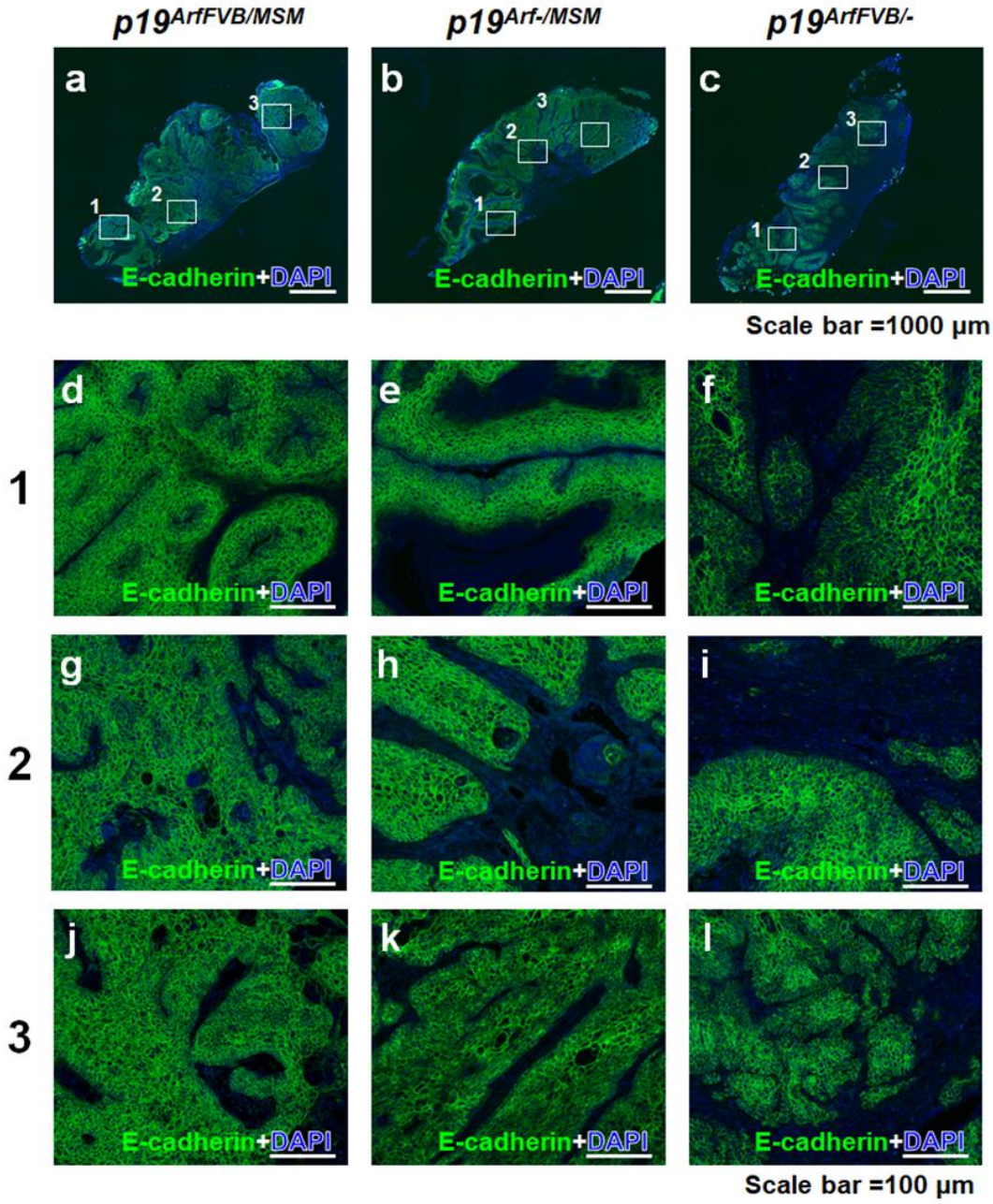

Figure 13. Immunostaining pattern of E-cadherin in carcinomas. (a-l) Immunostaining patterns of E-cadherin (green) in carcinomas from *p19*$^{Arf\ FVB/MSM}$, *p19*$^{Arf\ -/MSM}$, and *p19*$^{Arf\ FVB/-}$ mice. (d-l) are magnified regions in white boxes in (a-c). Cells were counterstained with DAPI (blue). Scale bars=1,000 μm (a-c), 100 μm (d-l).

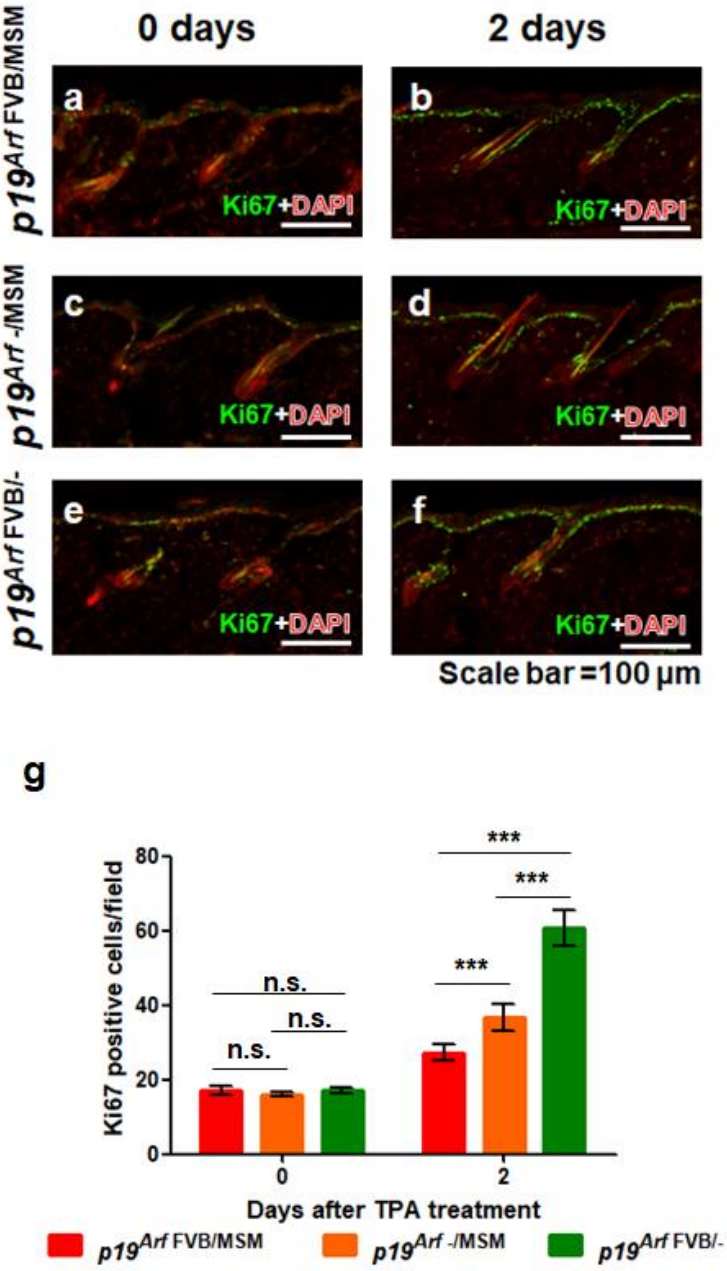

Figure 14. The *p19*$^{Arf\ MSM}$ allele reduces proliferating cells in mouse skin after TPA treatment. (a-f) Immunostaining patterns of Ki67 (green) in skin from (a, b) *p19*$^{Arf\ FVB/MSM}$, (c,d) *p19*$^{Arf\ -/MSM}$, and (e, f) *p19*$^{Arf\ FVB/-}$ mice (0 and 2 days after TPA treatment). (g) The number of Ki67-positive cells in papillomas from a *p19*$^{Arf\ FVB/MSM}$ (n=7) (red bars), *p19*$^{Arf\ -/MSM}$ (n=7) (orange bars), and *p19*$^{Arf\ FVB/-}$ mice (n=7) (green bars). The *P*-value for number of Ki67-positive cells was calculated by two-way ANOVA (***P<0.001). n.s., not significant. Error bars represent the standard deviation (S.D.).

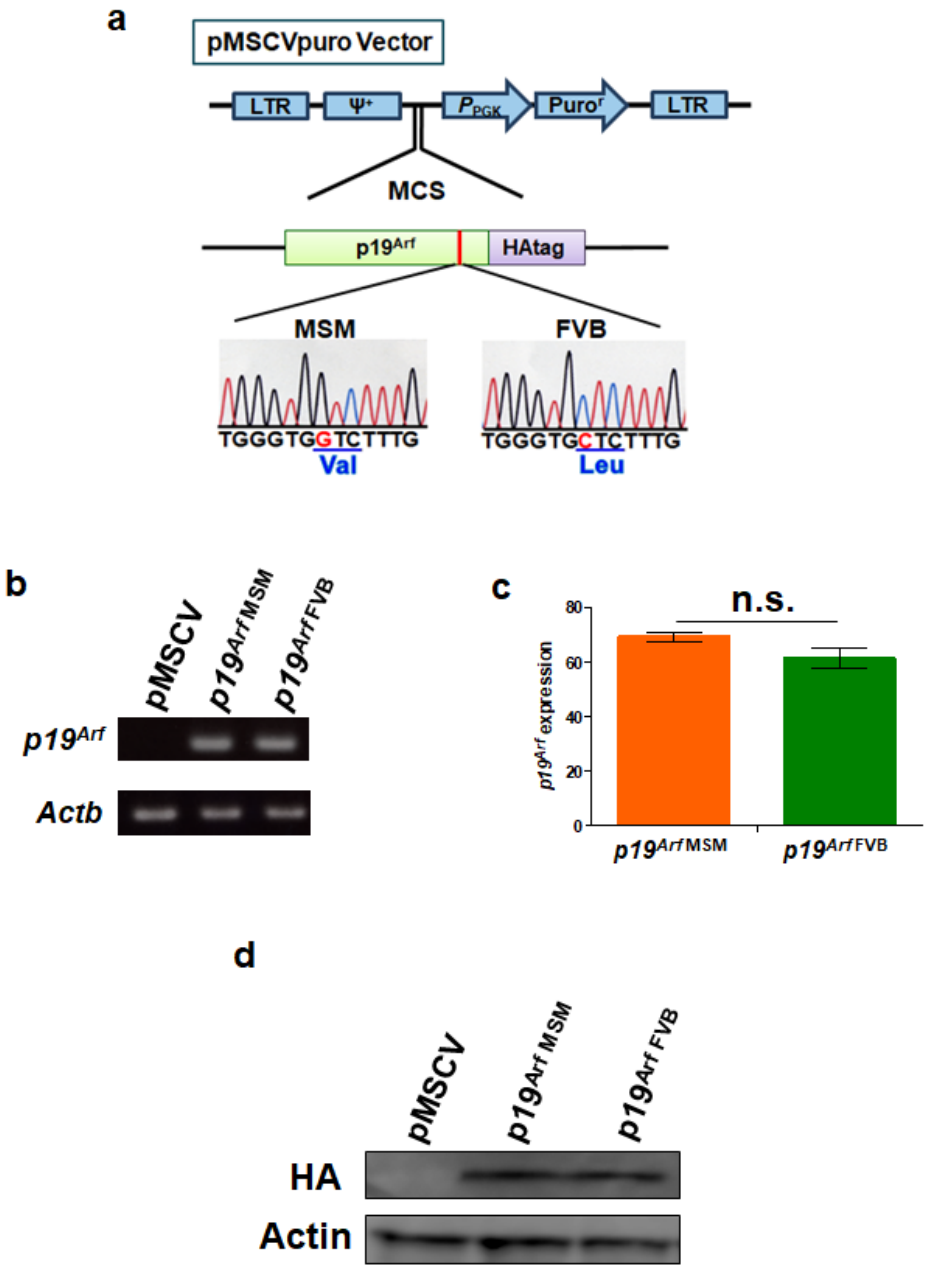

Figure 15. Generation of NIH/3T3 cells overexpressing *p19*$^{Arf\ MSM}$ or *p19*$^{Arf\ FVB}$. (a) A schematic drawing of *p19*^{Arf}-HA constructs for each allele. (b,c) *p19*^{Arf} mRNA expression levels detected by (b) RT-PCR and (c) qRT-PCR analysis using NIH/3T3 cells 2 days after infection. (d) p19^{Arf} protein expression levels measured by Western blot analysis using NIH/3T3 cells 2 days after infection. Actin expression is shown as an internal control. Error bars represent the standard deviation (S.D.). n.s., not significant.

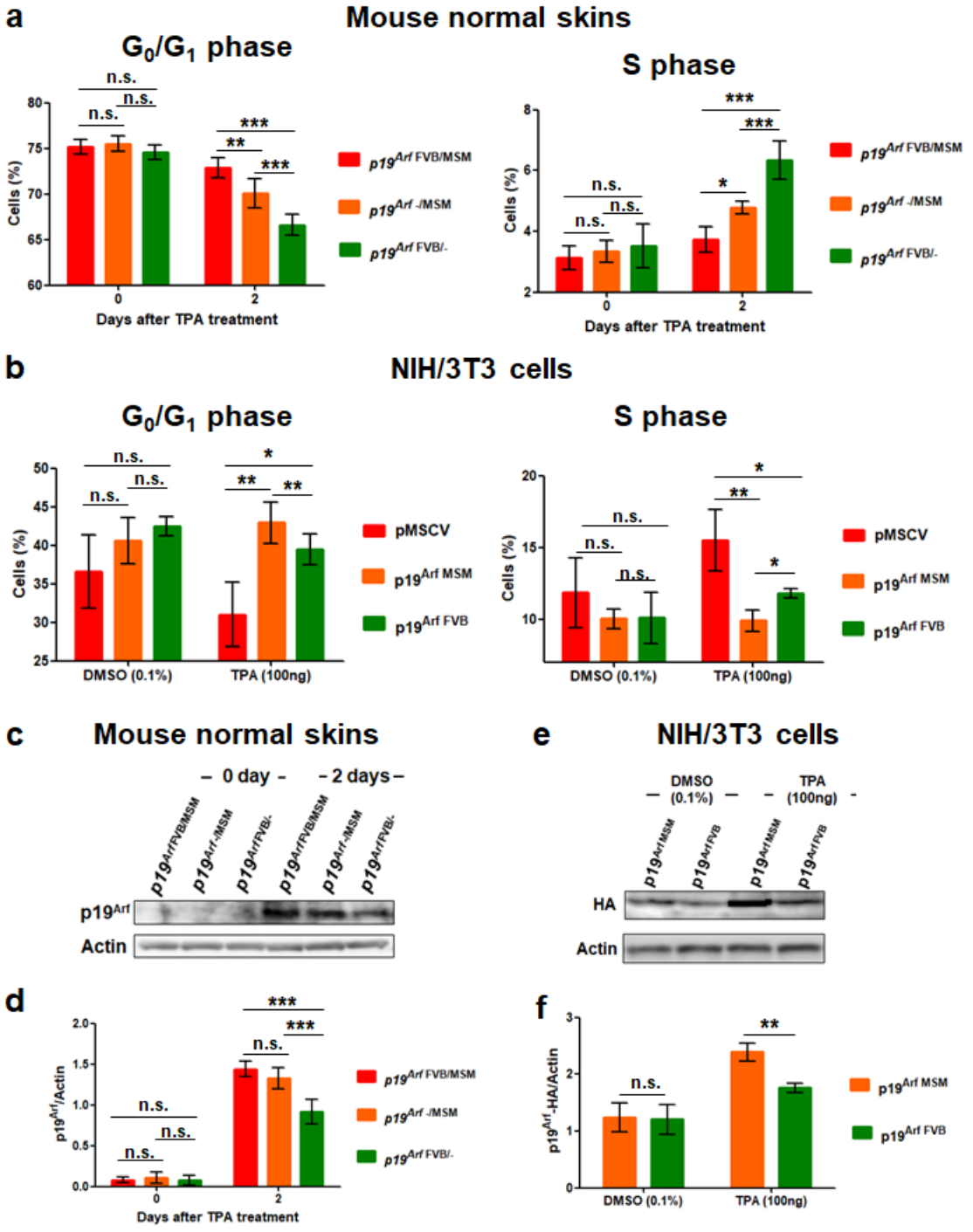

Figure 16. The *p19*$^{Arf\ MSM}$ allele is more effective in inducing G_1 arrest than the *p19*$^{Arf\ FVB}$ allele after TPA treatment. (a-b) Cell cycle analysis of MSM/Ms and FVB/N variants of *p19*^{Arf}. (a) TPA-treated skin from *p19*$^{Arf\ FVB/MSM}$ (n=4) (red bars), *p19*$^{Arf\ -/MSM}$ (n=4) (orange bars), and *p19*$^{Arf\ FVB/-}$ mice (n=4) (green bars) (0 day and 2

days after TPA treatment). (b) NIH/3T3 cells infected with a control vector (pMSCV) (n=3) (red bars), *p19*$^{Arf\ MSM}$ (n=3) (orange bars), or *p19*$^{Arf\ FVB}$ (n=3) (green bars) were treated with DMSO (0.01%) or TPA (100 ng). DNA content was measured by propidium iodide (PI) staining. (c-f) p19^{Arf} protein expression detected by western blot analysis and compared with the amount of p19^{Arf}. (c, d) TPA-treated skin from *p19*$^{Arf\ FVB/MSM}$ (n=5) (red bars), *p19*$^{Arf\ -/MSM}$ (n=5) (orange bars) and *p19*$^{Arf\ FVB/-}$ mice (n=5) (0 and 2 days after TPA treatment). (e, f) NIH/3T3 cells infected with *p19*$^{Arf\ MSM}$ (n=3) (orange bars) or *p19*$^{Arf\ FVB}$ (n=3) (green bars) were treated with DMSO (0.01%) or TPA (100 ng). Actin expression is shown as an internal control. The *P*-values were calculated by one- and two-way ANOVA (***P<0.001, **P<0.01, *P<0.05). n.s., not significant. Error bars represent the standard deviation (S.D.).

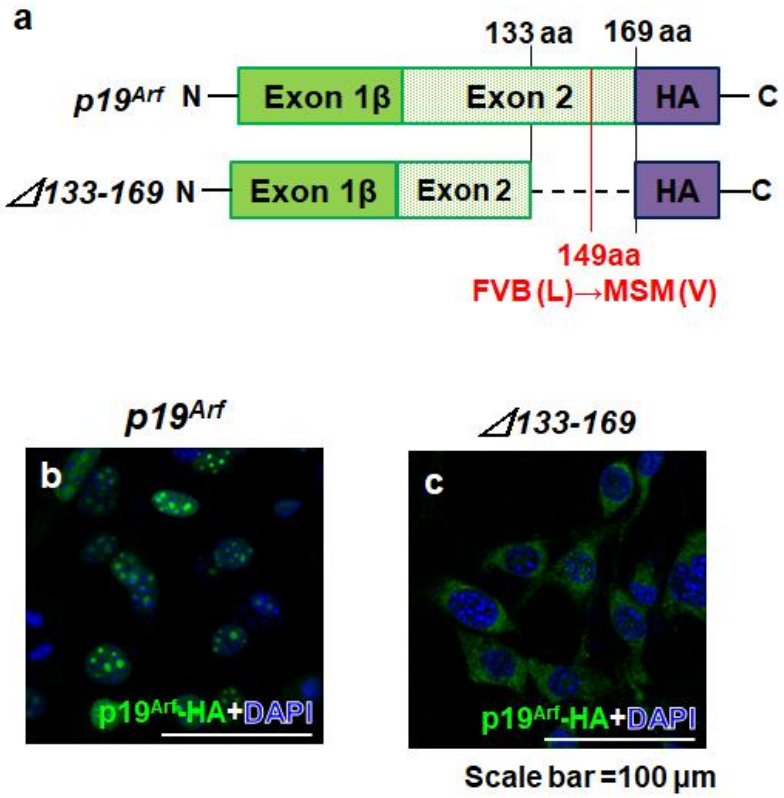

Figure 17. p19^{Arf} mutant lacking the C-terminal region is located in cytoplasm. (a) A schematic drawing of *p19^{Arf}*-HA mutant constructs (*⊿133-169*). Red line indicates the SNP in MSM/Ms (149 aa). (b, c) Immunostaining patterns of p19^{Arf}-HA (green) in NIH/3T3 cells. Cells were infected with *p19^{Arf}* and *⊿133-169*. Cells were counterstained with DAPI (blue).

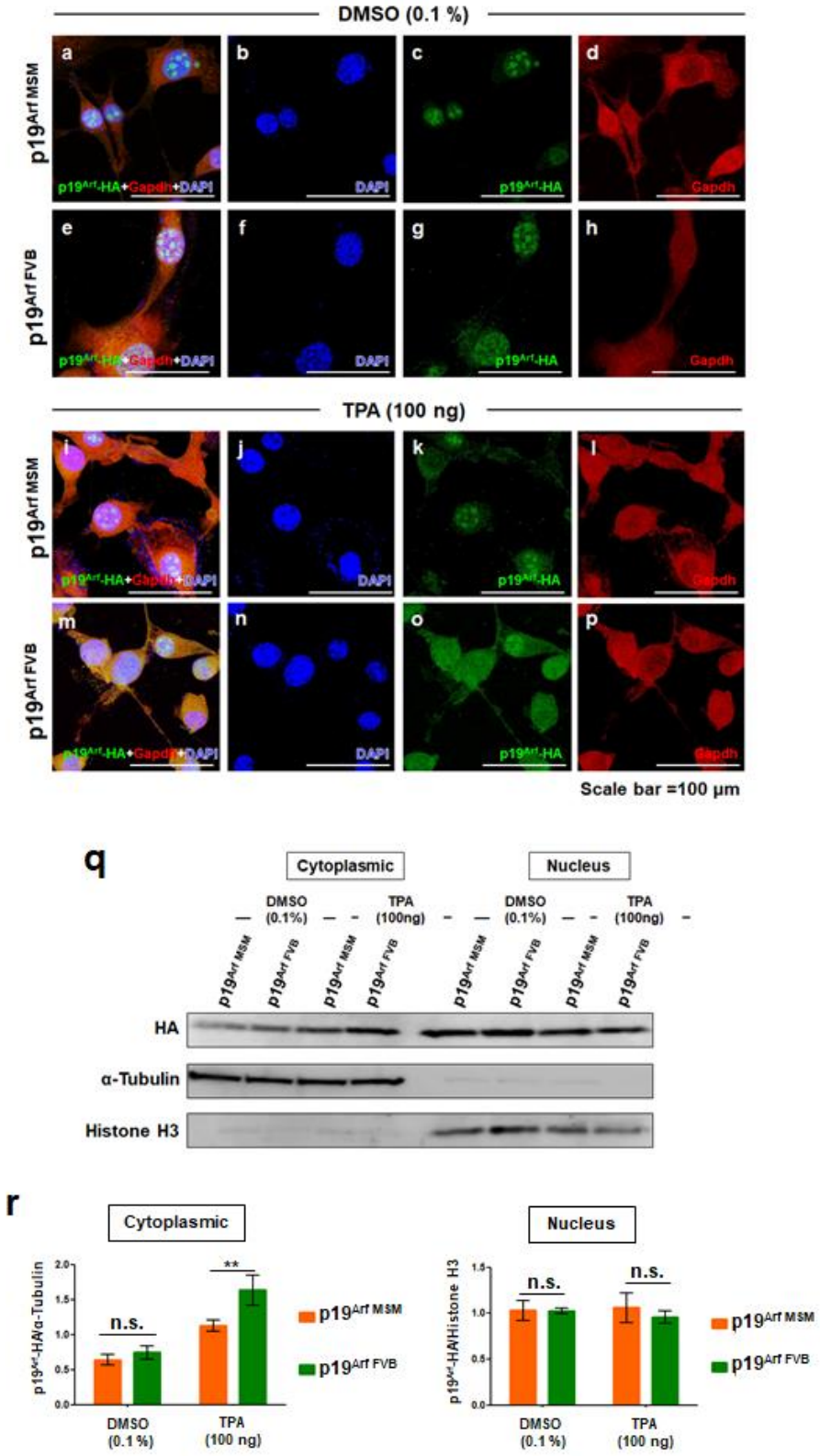

Figure 18. Genetic polymorphism of *p19^{Arf}* alters subcellular localization. (a-p) Double-immunostaining patterns of p19^{Arf}-HA (green) and Gapdh (red) in NIH/3T3

cells. Cells were infected with *p19*$^{Arf\ MSM}$ or *p19*$^{Arf\ FVB}$ and treated with DMSO (0.01%) or TPA (100 ng). Cells were counterstained with DAPI (blue). (q-r) Cytoplasmic and nuclear extracts from an equal number of cells treated with DMSO (0.01%) (n=3) or TPA (100 ng) (n=3). p19^{Arf} protein expression detected by Western blot analysis. α-Tubulin (cytoplasm) and Histone H3 (nucleus) expression is shown as an internal control. The *P*-values were calculated by one-way ANOVA (***P*<0.01, **P*<0.05). n.s., not significant. Error bars represent the standard deviation (S.D.).

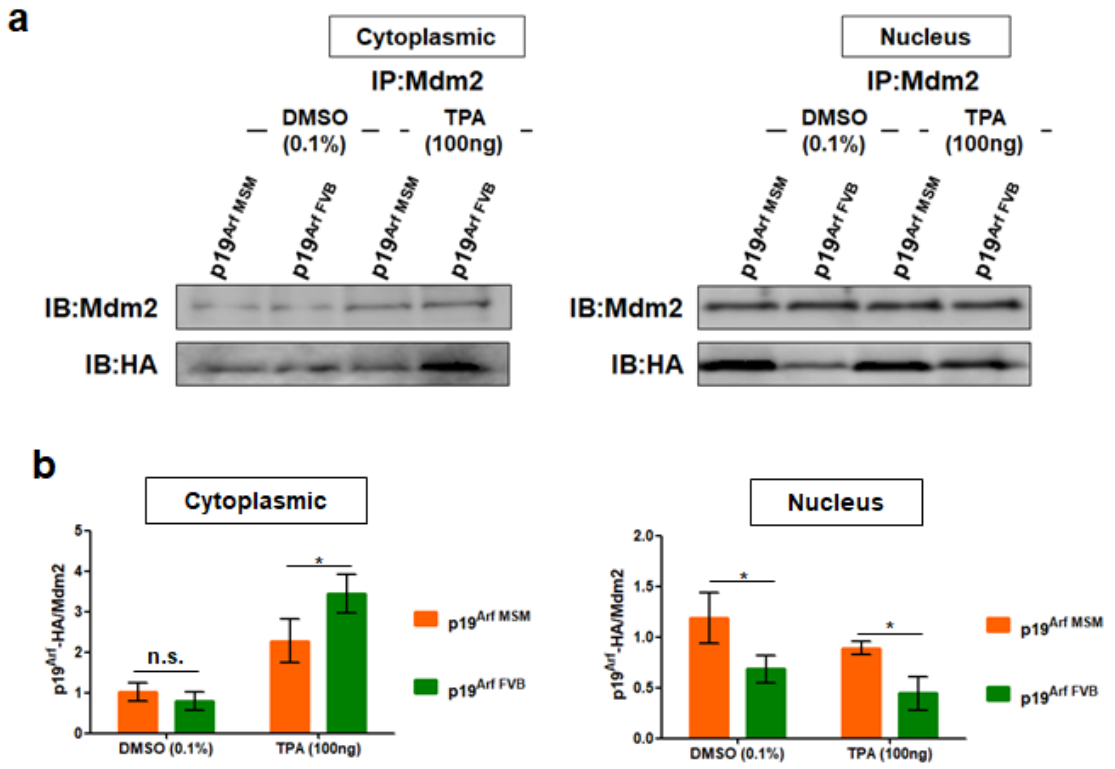

Figure 19. p19$^{Arf\ MSM}$ is mainly localized with Mdm2 in the nucleus. (a) NIH/3T3 cells were transfected with p19$^{Arf\ MSM}$-HA or p19$^{Arf\ FVB}$-HA and treated with DMSO (0.01%) or TPA (100 ng) (n=3). Immunoprecipitation (IP) with anti-MDM2 antibody, and subsequent immunoblotting analysis with anti-HA and anti-MDM2 antibodies. (b) The amounts of p19^{Arf} normalized by Mdm2. The *P*-values were calculated by one-way ANOVA (**P<0.01, *P<0.05). n.s., not significant. Error bars represent the standard deviation (S.D.).

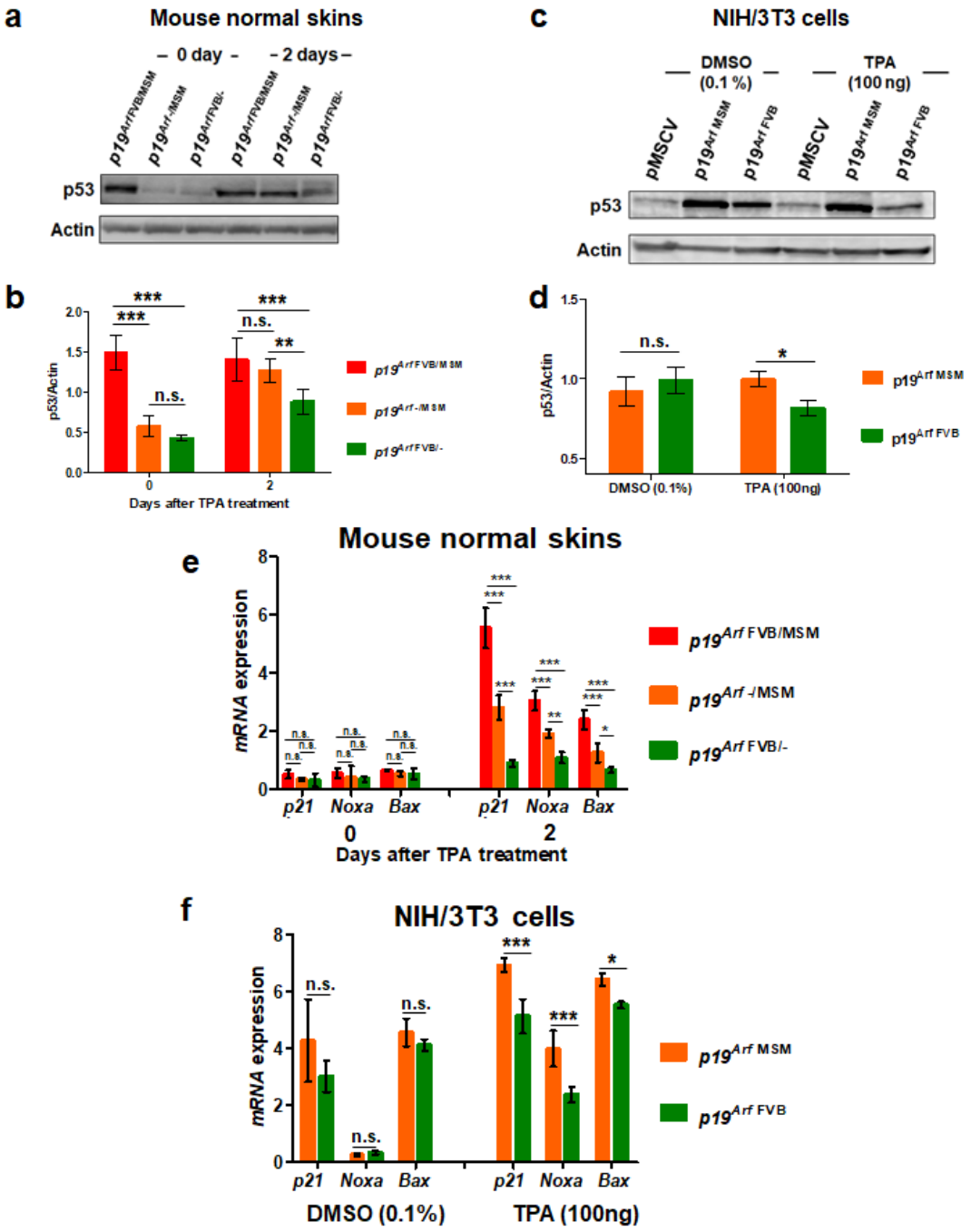

Figure 20. p19$^{Arf\ MSM}$ protein upregulates the expression of p53 and p53 target genes. (a-d) p53 protein expression detected by Western blot analysis and compared with the amount of p53. (a, b) TPA-treated skin from *p19*$^{Arf\ FVB/MSM}$ (n=5) (red bars), *p19*$^{Arf\ -/MSM}$ (n=5) (orange bars), and *p19*$^{Arf\ FVB/-}$ mice (n=5) (0 and 2 days after TPA treatment). (c, d) NIH/3T3 cells infected with *p19*$^{Arf\ MSM}$ (n=3) (orange bars) or *p19*$^{Arf\ FVB}$ (n=3) (green bars) were treated with DMSO (0.01%) or TPA (100 ng). Actin

expression is shown as an internal control. (e, f) mRNA expression levels of p53 target genes (*p21*, *Noxa*, and *Bax*). (e) qRT-PCR analysis of TPA-treated skin from $p19^{Arf\ FVB/MSM}$ (n=3) (red bars), $p19^{Arf\ -/MSM}$ (n=3) (orange bars), and $p19^{Arf\ FVB/-}$ (n=3) (green bars) mice (0 and 2 days after TPA treatment). (f) qRT-PCR analysis of NIH/3T3 cells infected with $p19^{Arf\ MSM}$ (n=3) (orange bars) or $p19^{Arf\ FVB}$ (n=3) (green bars) treated with DMSO (0.01%) or TPA (100 ng). The *P*-values were calculated by one- and two-way ANOVA (***P<0.001, **P<0.01, *P<0.05). n.s., not significant. Error bars represent the standard deviation (S.D.).

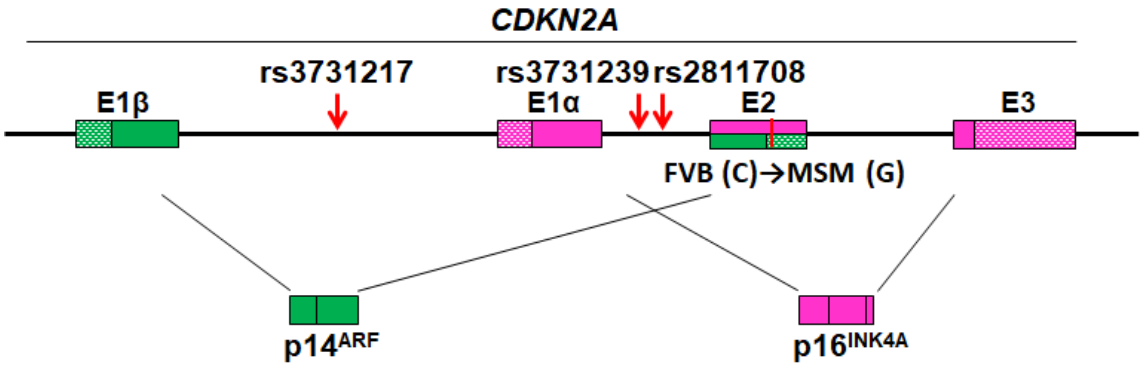

Figure 21. The location of SNPs in the *CDKN2A* locus. A schematic representation of the location of three SNP markers (rs2811708, rs3731217, rs3731239) in the *CDKN2A* locus. The red line represents the genetic variant between MSM/Ms (G) and FVB/N (C).

Table 1. Primers for off-target sites.

Chr	[a]Location (bp)	Primer name	Sequence (5'-3')	[b]Mutation
p16^{Ink4a} knockout mice				
13	113880603-113881085	Ch.13_F	CCGAGGTGGCTGGTGTCT	N.D.
		Ch.13_R	CAGGATGGAGATGGCCCT	
19	57581017-57581450	Ch.19_F	TCACTATGTTGTGGATGC	N.D.
		Ch.19_R	GCTAAGGCAGCACCACGT	
p19^{Arf} knockout mice				
8	34194827-34195350	Ch.8_F	GAGCTTCCCAGAGTCCGT	N.D.
		Ch.8_R	ATGGGTGTAACGTTCTAG	
9	107698919-107699393	Ch.9_F	CAGCTCATCTTGAATCCA	N.D.
		Ch.9_R	AGGCCTCTGAAGACCGGC	
18	38741970-38742006	Ch.18_F	CTGCACATGCTACCGCTT	N.D.
		Ch.18_R	TACACCTGGATCCTATGG	
3	33914436-33914926	Ch.3_F	GCCATTCTACGTGGAGAA	N.D.
		Ch.3_R	AGTCACCAGCTCACTGTG	
5	120493266-120493633	Ch.5_F	GGGCTCTGACCTGGCTCA	N.D.
		Ch.5_R	CCATTCATCTGTCAGTCT	
5	146435170-146435539	Ch.5_F2	GTATCAGCTTCTAGCCAA	N.D.
		Ch.5_R2	CCTCACAGTTGCCACTCA	
13	78203038-78203417	Ch.13_F2	CAGGTAGGACCCGGAGAA	N.D.
		Ch.13_R2	ACAGCTCTGCACGGCCAC	

[a]Amplified region. [b]N.D: not detected.

Table 2. Characteristics of study population

	Number of samples			Age (mean ± s.d.)		Female (%)	
	case	control	total	case	control	case	control
breast cancer	2,301	8,663	10,964	55.5 ± 10.4	62.1 ± 14.7	2,301 (100.0%)	8,663 (100.0%)
colorectal cancer	2,814	16,882	19,696	63.3 ± 10.8	62.6 ± 13.0	1,013 (36.0%)	8,663 (51.3%)
hepatic cancer	1,774	15,060	16,834	67.5 ± 8.9	62.6 ± 13.0	420 (23.7%)	7,926 (52.6%)
lung cancer	2,020	16,882	18,902	65.8 ± 9.4	62.6 ± 13.0	683 (33.8%)	8,663 (51.3%)
prostate cancer	1,756	8,191	9,947	69.0 ± 7.3	63.1 ± 10.9	0 (0.0%)	0 (0.0%)
stomach cancer	2,346	16,882	19,228	64.9 ± 9.1	62.6 ± 13.0	521 (22.2%)	8,663 (51.3%)

Table 3. Association of SNPs in the *CDKN2A* locus with 6 cancers

				breast cancer		colorectal cancer		hepatic cancer		lung cancer		prostate cancer		stomach cancer	
SNP	CHR	BP	[a]A1	OR (95% C.I.)	[b]P	OR (95% C.I.)	[c]P	OR (95% C.I.)	[c]P	OR (95% C.I.)	[b]P	OR (95% C.I.)	[b]P	OR (95% C.I.)	[c]P
rs2811708	9	21963422	T	1.15 (1.06-1.26)	0.00132	1.07 (0.99-1.15)	0.0822	1.01 (0.92-1.12)	0.8034	0.99 (0.91-1.08)	0.7910	0.98 (0.89-1.09)	0.7438	1.00 (0.93-1.09)	0.9543
rs3731239	9	21964218	C	0.98 (0.89-1.08)	0.62930	1.06 (0.98-1.15)	0.1296	0.96 (0.86-1.07)	0.4222	1.12 (1.02-1.22)	0.0145	1.09 (0.98-1.22)	0.1158	1.01 (0.92-1.10)	0.8607
rs2811709	9	21970151	A	1.10 (0.83-1.45)	0.50670	1.12 (0.90-1.40)	0.2955	0.83 (0.60-1.17)	0.2893	1.13 (0.87-1.45)	0.3627	0.76 (0.54-1.07)	0.1110	1.02 (0.80-1.31)	0.8616
rs4074785	9	21971583	T	0.97 (0.86-1.10)	0.64540	0.91 (0.82-1.01)	0.0751	0.87 (0.76-1.00)	0.0547	1.02 (0.91-1.15)	0.7400	0.94 (0.82-1.09)	0.4078	0.96 (0.86-1.07)	0.4770
rs3731217	9	21974661	G	1.15 (1.06-1.26)	0.00151	1.07 (1.00-1.16)	0.0573	1.05 (0.95-1.16)	0.3259	0.97 (0.89-1.06)	0.5189	1.04 (0.94-1.15)	0.4727	1.00 (0.92-1.09)	0.9545

[a] A1 alleles were considered as effect alleles. [b,c] P-values were calculated by logistic regression analysis using [b,c]age and [c]gender as covariates. OR: odds ratio, 95% C.I.: 95% confidence interval.

Journal of Investigative Dermatology., doi: 10.1016/j.jid.2018.12.027.

平成 31 年 1 月 23 日　　オンライン公表済